NASA Technical Memorandum 84319

Unsteady Laminar Boundary-Layer Calculations on Oscillating Configurations Including Backflow
Part II: Airfoil in High-Amplitude Pitching Motion — Dynamic Stall

W. Geissler

July 1983

NASA
National Aeronautics and
Space Administration

NASA Technical Memorandum 84319

Unsteady Laminar Boundary-Layer Calculations on Oscillating Configurations Including Backflow Part II: Airfoil in High-Amplitude Pitching Motion — Dynamic Stall

W. Geissler, Ames Research Center, Moffett Field, California

National Aeronautics and
Space Administration

Ames Research Center
Moffett Field, California 94035

Page intentionally left blank

Page intentionally left blank

TABLE OF CONTENTS

Page

LIST OF SYMBOLS v

SUMMARY 1

INTRODUCTION 1

INVISCID VELOCITY DISTRIBUTION OBTAINED BY A PANEL METHOD 2

UNSTEADY LAMINAR BOUNDARY-LAYER EQUATIONS 3

INITIAL CONDITIONS 5
  Conditions at $x_1 = \Delta x$, for all $\bar{T}$ 5
  Conditions at $\bar{T} = \bar{T}_0$ for all x_1 6

UNSTEADY FINITE-DIFFERENCE PROCEDURE 7

SEPARATION AND REATTACHMENT LINES 7

RESULTS 8
  Case A: $\alpha = 0° + 8° \sin \omega^* T$ 8
  Case B: $\alpha = 8° + 8° \sin \omega^* T$ 9
  Case C: $\alpha = 16° + 8° \sin \omega^* T$ 11

CONCLUSION 11

REFERENCES 13

FIGURES 15

LIST OF SYMBOLS

c, ε, p	constant values for initial (time-dependent) conditions
c_f	skin-friction coefficient
d	displacement amplitude of stagnation point movement
f	frequency
ℓ	reference length (airfoil chord)
p	pressure
$Re = U_\infty \ell/\nu$	Reynolds number
s	surface coordinate
$T = tU_\infty/\ell$	dimensionless time
$\bar{T} = T/(2\pi/\omega^*)$	normalized time
t	time
U_{kin}	kinematic velocity of the stagnation point referred to U_∞
$U(x,t), U_1(x_1,t)$	Outer inviscid velocity distribution referred to U_∞
U_∞	undisturbed main-flow velocity
$u(x,t), v(x,t)$	velocity components inside the boundary layer (profile-fixed system) referred to U_∞
$u_1(x_1,t), v_1(x_1,t)$	velocity components (stagnation-point fixed system) referred to U_∞
x, y	profile-fixed coordinate system (along the airfoil surface)
x_1, y_1	stagnation-point-fixed coordinate system (along the airfoil surface)
x_0	steady mean position of stagnation point
$\alpha = \alpha_0 + \alpha_1 \sin \omega^* T$	time-dependent incidence
α_0	steady mean incidence
α_1	oscillation amplitude
$\Delta x, \Delta y, \Delta T$	step-sizes in x-, y-, and T-directions
δ_1	boundary-layer displacement thickness
ν	kinematic viscosity

τ_w	wall shear-stress
$\omega^* = 2\pi f \ell / U_\infty$	reduced frequency

UNSTEADY LAMINAR BOUNDARY-LAYER CALCULATIONS ON OSCILLATING CONFIGURATIONS INCLUDING BACKFLOW

PART II: AIRFOIL IN HIGH-AMPLITUDE PITCHING MOTION — DYNAMIC STALL

W. Geissler*

Ames Research Center

SUMMARY

A previously developed finite-difference procedure for calculating unsteady, incompressible, laminar boundary layers on an oscillating flat plate is applied to a wing section undergoing high-amplitude pitching oscillations about various mean incidences. To start the entire boundary-layer calculation, appropriate initial conditions and outer boundary conditions are specified, using a stagnation-point fixed frame of reference. The breakdown of the numerical calculation procedure in the x,t-domain is interpreted to coincide with unsteady separation. Details of the boundary-layer behavior in the vicinity of separation are investigated, and a close analogy between the present results and those for a three-dimensional steady separation is found.

INTRODUCTION

The experimental and analytical investigation of unsteady flow separation on oscillating helicopter rotor blades, known as dynamic stall, has been of great concern in recent years. A comprehensive treatment of this problem on the basis of unsteady laminar and turbulent boundary-layer calculations was given by McCroskey and Philippe (ref. 1). A large amount of experimental data — obtained in studies of seven helicopter airfoil sections, including pressures and forces, as well as hot-wire and hot-film data — are included in reference 2. Some detailed unsteady pressure measurements on oscillating three-dimensional-blade tips with various planforms, including a rectangular planform with a NACA 0012 airfoil section, have been made in the low-speed, 3- by 3-m wind tunnel of the DFVLR in Goettingen as part of a joint NASA/DFVLR cooperation program (ref. 3).

The most important and least understood problems associated with these complicated, unsteady viscous flows occur in regions of time-dependent reversed flow along the wing surface. These regions are, therefore, the main concern in the present study.

It has already been shown in the first part of the present analytical investigation (ref. 4) that a numerical calculation procedure based on finite differences can be extended in a straightforward manner into regions of backflow on an oscillating surface. Although stability considerations (the CFL condition) limit the region

---

*NRC, Deutsche Forschungs- und Versuchsanstalt für Luft- und Raumfahrt, Forschungbereich Werkstoffe und Bauweisen.

over which the boundary-layer calculation can actually be extended, in the flat-plate case calculations could be continued into parts of the flow with strong back-flow velocities without severe numerical problems.

In the present work, the same calculation procedure will therefore be used to treat the unsteady, laminar boundary-layer equations on oscillating airfoils. The aim of the calculation is to investigate in detail the unsteady separation phenomenon by following the behavior of characteristic boundary-layer quantities, such as velocity and vorticity distributions inside the boundary layer, and the development of wall shear-stress and boundary-layer displacement thickness in the x,t-domain.

The same numerical method that has been applied in the present calculation has also been used to solve the laminar, three-dimensional boundary-layer equations over blunt bodies of revolution (ref. 5). It has been pointed out by different investigators (refs. 6 and 7) that a close relationship exists between two-dimensional-unsteady and three-dimensional-steady boundary layers. Thus, there will be some emphasis on this problem by way of comparing the previously obtained three-dimensional-steady results with the present unsteady data.

The two-dimensional cases studied herein are concentrated on the NACA 0012 airfoil section pitching about its quarter-chord axis. The steady mean angle of incidence is changed from 0° to 16° with an 8° oscillation amplitude. In addition to the quasi-steady case, reduced frequencies of $\omega^* = 0.2$ and $\omega^* = 0.4$ have been treated.

The work reported herein was performed while the author was an NRC Postdoctoral Fellow at NASA Ames Research Center. The use of computer facilities at Ames Research Center under the auspices of the Aerodynamics Research Branch is gratefully acknowledged.

INVISCID VELOCITY DISTRIBUTION OBTAINED BY A PANEL METHOD

A three-dimensional, unsteady panel-method was developed (ref. 8) to calculate the steady and first-harmonic unsteady air loads on oscillating wing configurations. Results of this method have been compared with many experimental data (refs. 3 and 9) for different airfoil geometries, incidences, and frequencies. It has been shown that the panel method is an accurate and computer- time-efficient tool for determining steady and unsteady air loads on three-dimensional configurations.

In the present case, the unsteady panel-method has been applied to a rectangular wing, with an aspect ratio of $\Lambda = 4$ and a NACA 0012 airfoil section, pitching about its quarter-chord axis. For this configuration, extensive steady and unsteady experimental data have been obtained in the 3- by 3-m, low-speed wind tunnel at DFVLR-AVA, Goettingen. The experimental work formed part of a NASA-Langley/DFVLR joint program on the investigation of unsteady air loads on oscillating helicopter rotor-blade tips with different planforms.

Corresponding to the experimental data three angles of incidence have been used in the following viscous calculations:

$$\text{Case A:} \quad \alpha = 0° + 8° \sin \omega^* T \tag{1a}$$

$$\text{Case B:} \quad \alpha = 8° + 8° \sin \omega^* T \tag{1b}$$

$$\text{Case C:} \quad \alpha = 16° + 8° \sin \omega^* T \tag{1c}$$

corresponding to no stall, light dynamic stall, and deep dynamic stall conditions, respectively.

The inviscid velocity distributions will be used as outer boundary conditions for calculating the unsteady, two-dimensional laminar boundary layer on a wing section at $y/s = 0.25$ ($\Lambda = 4$), where the flow is assumed to be quasi-two-dimensional. Figures 1-3 show the velocity distributions on the upper surface for the three incidence cases (cases A-C) as functions of the surface coordinate x_1 and the dimensionless time $\bar{T}$ ($\bar{T} = T_0\omega^*/2\pi$) within a period of oscillation. The velocity has been referred to a coordinate system which is fixed to the moving, front stagnation point of the wing section.

All three incidence cases show very steep spatial velocity-gradients over parts of the oscillatory cycle but those are completely reduced over other parts of the cycle in the two lower mean-incidence flows (figs. 1 and 2). The velocity gradients remain large over the whole cycle for the highest mean incidence case (fig. 3).

For the following boundary-layer calculations the inviscid velocity distributions remain unchanged.

UNSTEADY LAMINAR BOUNDARY-LAYER EQUATIONS

In a body-fixed frame of reference, the unsteady laminar boundary-layer equations for continuity and momentum are, respectively,

$$\frac{\partial u}{\partial x} + \frac{\partial v}{\partial y} = 0 \tag{2}$$

$$\frac{\partial u}{\partial t} + u\frac{\partial u}{\partial x} + v\frac{\partial u}{\partial y} = -\frac{1}{\rho}\frac{\partial p}{\partial x} + \nu\frac{\partial^2 u}{\partial y^2} \tag{3}$$

with the boundary conditions

$$\left.\begin{aligned} y = 0\ , &\quad u = v = 0 \\ y \to \infty\ , &\quad u = U(x,t) \end{aligned}\right\} \tag{4}$$

The outer inviscid velocity $U(x,t)$ is determined by the unsteady panel-method discussed in the previous section.

To start the unsteady boundary-layer calculation on an oscillating profile one has to take into account the time-dependent movement of the stagnation point. If the calculation is performed in a body-fixed frame of reference, special treatment of the stagnation-point region is necessary to get the boundary-layer calculation properly started (ref. 10). These complications have been reduced by working in a stagnation-point-fixed frame. From the inviscid velocity distribution, the time-dependent location of the stagnation point can be specified. Figure 4 shows the movement of the stagnation point in body-fixed coordinates for the incidence case A, in which $\alpha = 0° + 8° \sin \omega^* T$. This time dependency is nearly harmonic and is 180° out of phase with respect to the angle of incidence. The amplitude of the displacement is $d = 0.01825$ for this special case.

Assuming that the stagnation point is always located on the body surface ($y = 0$), one can start the unsteady boundary-layer calculation for both lower and upper surfaces from the instantaneous position of the stagnation point. A transformation of the boundary-layer equations and boundary conditions (eqs. (2)-(4)) into a stagnation-point-fixed frame of reference is straightforward.

The coordinate along the wall, measured from the stagnation point, can be expressed by

$$x_{1u} = x - x_0 + d\, e^{i\omega^* T} \qquad \text{(upper surface)} \tag{5}$$

$$x_{1\ell} = -(x - x_0) - d\, e^{i\omega^* T} \qquad \text{(lower surface)} \tag{6}$$

(ω^* = reduced frequency, T = dimensionless time)

with x_0 as the steady mean position of the stagnation point. The normal coordinate $y_1 = y$ remains unchanged.

With

$$U_{1kin} = \frac{\partial x_1}{\partial t} = \pm i\omega^* \, d\, e^{i\omega^* T} \tag{7}$$

as the kinematic velocity in the stagnation-point-fixed system (the ± signs refer to the upper (+) and lower (-) surfaces), the velocity component in the x_1-direction is transformed:

$$\left.\begin{aligned} u_1 &= u + U_{kin} \\ v_1 &= v \end{aligned}\right\} \tag{8}$$

Inserting expressions (7) and (8) into boundary-layer equations (2) and (3) one obtains

$$\frac{\partial u_1}{\partial x_1} + \frac{\partial v_1}{\partial y_1} = 0 \tag{9}$$

$$\frac{\partial u_1}{\partial t} + u_1 \frac{\partial u_1}{\partial x_1} + v_1 \frac{\partial u_1}{\partial y_1} = \frac{\partial U_1}{\partial t} + U_1 \frac{\partial U_1}{\partial x_1} + \nu \frac{\partial^2 u_1}{\partial y_1^2} \tag{10}$$

With the boundary conditions

$$\left.\begin{aligned} y_1 &= 0\,, & u_1 &= \pm U_{1kin} = \pm i\omega^*\, d\, e^{i\omega^* T} \\ y_1 &\to \infty\,, & u_1 &= U[x_1(x,t),t] \pm U_{1kin} = U_1 \pm i\omega^*\, d\, e^{i\omega^* T} \end{aligned}\right\} \tag{11}$$

There is formally no difference between these systems in the boundary-layer equations themselves; however, differences do show up in the boundary conditions. Specifically, the function $U[x_1(x,t),t]$ must be carefully specified within the new coordinate system. Figures 5(a) and 5(b) show the development of the inviscid velocity distribution over a period of oscillation for different distances from the stagnation point ($x_1 = 0$) in the zero-mean-incidence case.

Figure 6 shows the stagnation-point movement for incidence case, B, $\alpha = 8^\circ + 8^\circ \sin \omega^* T$, and two reduced frequencies: $\omega^* = 0.201$ and 0.4. The time-dependent movement looks similar to that in the previous case, with correspondingly larger amplitude. The influence of reduced frequency on the movement is small in contrast with the overall pressure distribution. Figure 7 shows the corresponding *time-dependent, inviscid velocity distribution in the stagnation-point frame of* reference.

Figures 8 and 9 display the results for high-angle-of-incidence case C, $\alpha = 16^\circ + 8^\circ \sin \omega^* T$.

INITIAL CONDITIONS

To start the unsteady boundary-layer calculation, initial conditions have to be specified at the end of the first x_1-step for all $\bar{T}$ as well as at $\bar{T} = \bar{T}_0$ for all x_1.

Conditions at $x_1 = \Delta x$, for all $\bar{T}$

Following the ideas of Glauert (ref. 11), the set of boundary-layer equations (eqs. (9)-(10)) can be transformed into ordinary differential equations by the assumption that in the vicinity of the stagnation point the inviscid velocity $U_1(x_1,T)$ varies linearly with respect to the distance from the stagnation point and harmonically in time

$$U_1 = cx_1 + c\varepsilon x_1 \, e^{ip\omega^* T} \tag{12}$$

with c, ε, and p as constant values which still have to be specified.

The velocity components inside the boundary layer may then be described by

$$u_1 = cx_1 f'(\eta) + cx_1 \varepsilon \phi'(\eta) e^{ip\omega^* T} \tag{13}$$

and

$$\left.\begin{aligned} v_1 &= -\sqrt{c}\left[f(\eta) + \varepsilon\phi(\eta) e^{ip\omega^* T}\right] \\ \eta &= y_1 \sqrt{c} \end{aligned}\right\} \tag{14}$$

It is easily shown that equations (13) and (14) fulfill continuity equation (9). Using expressions (13) and (14) in the boundary-layer equations (11) yields, for the steady part,

$$f''' + f'^2 + ff'' + 1 = 0 \tag{15}$$

as the stagnation-point case of the Falkner-Skan series with the boundary conditions

$$\eta = 0 \,, \qquad f = f' = 0$$

$$\eta \to \infty \,, \qquad f' = 1$$

and for the unsteady part

$$\phi''' - 2f'\phi' + f\phi'' + \phi f'' - \frac{ip\omega^*}{c}\,\phi' + \frac{ip\omega^*}{c} + 2 = 0 \tag{16}$$

with the boundary conditions for the complex function ϕ

$$\eta = 0\ , \qquad R(\phi) = \mathscr{I}(\phi) = R(\phi') = 0\ , \qquad \mathscr{I}(\phi') = \pm\,\frac{\omega^* d}{c x_1 \varepsilon}$$

$$\eta \rightarrow \infty\ , \qquad R(\phi') = 1\ , \qquad \mathscr{I}(\phi') = 0$$

($R(\phi)$ = Real part (ϕ), $I(\phi)$ = imaginary part (ϕ))

For the solution of the ordinary differential equations (15) and (16), a fourth-order Runge-Kutta solution procedure has been used; it is described in detail in reference 11. Figure 10 shows a typical result for the functions f' and ϕ' for the cases $\omega^*/c = 0$ (quasi-steady) and $\omega^*/c = 1$, 2, and 3. In the $R(\phi')$-curve the typical overshoot to values larger than 1 can be observed.

Before the calculation of the time-dependent, initial-velocity profiles can actually be carried out, the constants c, ε, and p in equation (12) must be determined. Figure 5(a) shows that (for the case of $\alpha = 0° + 8° \sin \omega^* T$) close to the stagnation point $U_1(T)$ is varying like a second harmonic with respect to $\alpha(T)$. This can be taken into account simply by setting $p = 2$ in equation (12). The best fit with the given $U_1(T)$ values for $x_1 = 0.002$ is obtained with $c = 60.5$ and $\varepsilon = 0.3305$. The dashed line in figure 5(a) shows the corresponding initial velocity distribution of this best fit. Figure 7 shows the distribution for case B, $\alpha = 8° + 8° \sin \omega^* T$. In case B, the prescribed velocity distribution behaves like a first harmonic ($p = 1$) with 180° phase shift. The best fit at $x_1 = 0.001$ is obtained with the constants $c = 42.6$ and $\varepsilon = -0.88$; at $x_1 = 0.004$, the best fit is obtained with $c = 47.5$ and $\varepsilon = -0.658$.

In case C — the high-angle-of-incidence case, $\alpha = 16° + 8° \sin \omega^* T$ — the constants at $x_1 = 0.001$ are $c = 24$ and $\varepsilon = -0.667$ (fig. 9).

Conditions at $\bar{T} = \bar{T}_0$ for all x_1

To start the calculation at arbitrary times $\bar{T}_0$ during the cycle, quasi-steady initial conditions have to be calculated. This is carried out by a two-dimensional finite-difference procedure, which takes into account the corresponding instantaneous inviscid velocity distribution at $\bar{T} = \bar{T}_0$ as outer boundary condition. The numerical method for this two-dimensional procedure is the same as the two-dimensional unsteady method which is described in detail in reference 4 and which is used with only minor changes for the present unsteady boundary-layer calculations as well. Figure 11 shows a result for case A ($\alpha = 0° + 8° \sin \omega^* T$). Wall shear-stress and boundary-layer displacement thickness are plotted versus x_1 at $\bar{T} = 0$. For comparison, the corresponding results obtained by a steady integral method (ref. 12) using the same outer boundary condition, are also displayed.

Figure 11(a) shows some characteristic numerical oscillations of τ_w which do not attenuate with increasing x_1. This behavior has already been observed for three-dimensional, steady boundary-layer calculations (ref. 13). Some uncertainties are obviously induced at the initial position. To overcome these oscillations, a simple iteration procedure has been applied with a linear interpolation of the boundary-layer profiles over three mesh points in the x_1-direction. Figure 11(b) shows the final result after this interpolation; the oscillations of τ_w are completely suppressed. The results are now in very good agreement with the data obtained by the integral method.

The interpolation procedure has also be applied in the unsteady calculations.

UNSTEADY FINITE-DIFFERENCE PROCEDURE

Details of the finite-difference method have already been outlined in reference 4. This Crank-Nicolson-type method, which is second-order accurate, proved to be sufficient and accurate for the oscillating flat-plate problem; it is used in the present case without changes. Restrictions with respect to numerical stability are taken into account (CFL condition). It was shown in reference 4 that the calculation can be continued into reversed-flow regions with zero spatial pressure gradient as long as the CFL condition is not violated. One aim of the present investigation is to explore the behavior of the unsteady boundary layer with spatial pressure gradient, specifically in regions of reversed flow.

After the initial and outer boundary conditions have all been specified, the numerical calculation over the entire x_1-$\bar{T}$ range can start. At $\bar{T} = \bar{T}_0 + \Delta\bar{T}$ the calculation progresses from the point $x_1 = \Delta x$ in the x_1-direction to x_{1max} and is then repeated at the next time-step. For simplicity, the Δx and ΔT step-sizes, as well as Δy through the boundary layer, are kept constant. The Δy step-size is doubled as soon as the number of grid points through the boundary layer exceeds 100. The calculation stops at a given time $\bar{T}_1$ such that $\bar{T}_1 = \bar{T}_0 + 1$ is one period. It has been found that in the present cases it was sufficient to stop the calculations after the first cycle.

SEPARATION AND REATTACHMENT LINES

A question of particular interest in the present study is where to stop the boundary-layer calculation in the x_1-direction. It was mentioned in the previous section that violation of the CFL condition is an indicator for limiting the calculation domain. However, it should be noted that this violation of the CFL condition is caused by the behavior of boundary-layer quantities, specifically the normal velocity inside the boundary layer as the solution approaches breakdown. As will be discussed in detail in the next section, this sudden breakdown of the numerical calculation over parts of the cycle indicates separation. It is not difficult to follow the corresponding separation boundaries, as long as those boundaries are extended from higher to lower x_1-positions during the marching process in time. Problems occur, however, in the reattachment zone, a result of a lack of information about this region from previous time-steps. Therefore, a simple procedure was developed to overcome this problem. Whenever the unsteady calculation reaches the maximum x_1-position with a positive wall shear-stress value, the boundary-layer calculation is continued on a quasi-steady basis. The quasi-steady calculation is extended until the wall shear-stress tends to zero. In the next time-step, the additional (quasi-steady) points are taken into account in the unsteady calculations, etc.

This procedure does not give the physically correct reattachment line, but it does allow the calculation to be continued over a complete cycle of oscillation. It was found that uncertainties along the reattachment line have only minor influences on the forward-moving separation region, which was the main concern in the present investigation.

RESULTS

Case A: $\alpha = 0° + 8° \sin \omega^*T$

Figures 12-19 show results of the unsteady boundary-layer calculation for the zero mean-incidence case. Close to the front stagnation point, the wall shear-stress τ_w is changing very rapidly with both x_1 and T (figs. 12 and 14) corresponding to the steep inviscid velocity peak at that position. To check the validity of the numerical method, quasi-steady results are included which show only minor differences within this region.

A similarly close correspondence is observed for the boundary-layer displacement thickness δ_1. Some oscillations did occur in the numerical results of τ_w versus x_1 (fig. 12) and δ_1 versus time (fig. 15), but they were removed by the iteration procedure described in the section on initial conditions (not shown).

Marching farther downstream, a position is reached where flow reversal occurs for the first time; no evidence of separation appears. Figure 16 shows some typical velocity profiles at the beginning of backflow.

Figures 17 and 18 display wall shear-stress and boundary-layer displacement thickness at different time-levels up to the point at which the numerical calculation breaks down. This breakdown occurs very suddenly and appears to be a violation of the CFL condition. Before the breakdown, the slopes of both the τ_w- and δ_1-curves are steepening considerably. The breakdown positions are indicated in figures 17 and 18 by end lines.

Strong deviations between quasi-steady and unsteady results are now apparent in the sense that the unsteady calculation can be extended beyond the points of quasi-steady separation.

Figure 19 shows the whole domain of unsteady boundary-layer calculations for the two frequency cases $\omega^* = 0.201$ and 0.400; the quasi-steady separation line is included as reference. The circles ($\omega^* = 0.201$) and the triangles ($\omega^* = 0.4$) indicate the positions where the unsteady boundary-layer calculation approaches breakdown as a result of a violation of the CFL condition. On the reattachment side, some severe numerical uncertainties occur which could not completely be suppressed; they are obviously caused by the simple quasi-steady extrapolation procedure (preceding section). It has again been proved by recalculations with various mesh sizes and mesh-size ratios ($\Delta x/\Delta T$) that these uncertainties have no influence on the forward-moving separation region which is of main concern in the present study.

For the case $\omega^* = 0.201$, the region of reversed flow is indicated in figure 19. The effects of reduced frequency on the separation boundaries are such that with increasing ω^* the most downstream position of flow reversal is slightly reduced; the upstream moving separation is shifted in time and is strongly accelerated toward the leading edge; and the reattachment positions are shifted in time with increasing frequency. These tendencies are much more pronounced in the higher incidence cases.

In the corresponding experimental data (ref. 3) that have been obtained at a chord Reynolds number of 1.2 million, no sign of severe unsteady separation was observed; however, at a position close to the leading edge, a strong deviation from inviscid theoretical values for the unsteady first harmonic pressures indicated the presence of a separation bubble at that position. That bubble is presumed to be followed by attached turbulent flow over the remainder of the airfoil.

Case B: $\alpha = 8^\circ + 8^\circ \sin \omega^* T$

Figures 20-24 display results of τ_w and δ_1 for the higher mean incidence case of $\alpha_1 = 8^\circ$ on the upper surface of the profile. Figures 20 and 21 show the variations with respect to x_1 and figures 22 and 23 the variations with respect to time. Figure 24 gives the position of the upstream-moving separation and makes it possible to identify the various locations in figures 20-23. Again, the wall shear-stress initially goes negative without any sign of separation; however, the breakdown occurs abruptly. The breakdown points (indicated by the vertical dashed lines) move upstream very fast. The reason for the numerical breakdown of the boundary-layer calculation is clearly indicated in figures 22 and 23, which show τ_w and δ_1, respectively, versus time. The slopes of both τ_w and δ_1 progressively increase as breakdown is approached. An example of the steepness of the curves $(d\delta_1/d\tilde{T})$ is given in figure 23.

In the interest of gaining more insight into the flow behavior in the vicinity of unsteady (upstream moving) separation, figure 24 shows the breakdown points (circles), the location of zero wall shear-stress, and the quasi-steady separation line; the unit vectors of wall shear-stress in the x_1-$\bar{T}$-domain are also included.

A horizontal τ_w-vector indicates zero wall shear-stress. A vector pointing into the negative x_1-direction is an indicator of backflow. Equivalent to procedures that are used in three-dimensional flows, the slopes of the unsteady wall shear-stress vectors can be integrated forming "limiting streamlines" in the x_1-$\bar{T}$-domain; these lines are also included in figure 24. As in steady three-dimensional flow, the breakdown (separation) line coincides with an envelope of the limiting streamlines.

In the region where the acceleration of the forward-moving separation is very large, the τ_w-vectors turn very sharply, forming strongly curved limiting streamlines.

Figure 25 shows corresponding results obtained with a similar boundary-layer calculation procedure for a blunt body (spheroid) at incidence (ref. 14). The wall streamlines (fig. 25(b)) form an envelope beyond which the boundary-layer calculation breaks down. In front of the envelope, the wall shear-stress vectors are pointing to windward of the body, indicating reversed secondary flow on the entire body surface. The calculation was continued all over the body surface following the separation line to the rear. Figure 25(a) also gives the streamline coordinate mesh and the location of the separation line over the entire body surface.

A comparison of the separation characteristics of two-dimensional-unsteady and three-dimensional-steady flow gives evidence of a close analogy between both (this has already been pointed out by other investigators; refs. 6 and 7).

Figure 26 shows the separation lines for the quasi-steady case, as well as for the unsteady cases with $\omega^* = 0.201$ and $\omega^* = 0.400$ over the whole oscillatory cycle. Note the strong reduction of the maximum downstream position of separation with increasing frequency. Again (as in the zero-incidence case) the increasing frequency causes an increasing upstream acceleration of the separation point. This particular behavior of unsteady separation has also been observed in water-tunnel experiments (ref. 15).

Some numerical uncertainties in the reattachment region again show the difficulties associated with the simple, quasi-steady treatment of this region. The influences of these uncertainties died out with increasing time and were not noticeable in the region of forward-moving separation.

In the next sequence of figures (figs. 27-29) some characteristic boundary-layer quantities are plotted for the case $\omega^* = 0.2$ at a specific x_1-position which can be identified in figure 24. The three-dimensional plots, as well as the contour plots, are made over the $\bar{T}$-y_1-plane, showing the development in time through the whole boundary layer. At $\bar{T} = 1$, the boundary-layer calculation comes to the breakdown previously mentioned.

Figure 27(a) shows the behavior of the vorticity (only the term $\partial u/\partial y$ is displayed). Moving in time toward the separation line, the vorticity is forming a maximum away from the wall, and vorticity is spreading into the fluid. Figure 27(b) shows the steepening of equal vorticity lines approaching separation at $\bar{T} \doteq 1$. Vorticity lines not originating from the wall are observed close to separation.

Figures 28(a) and 28(b) give the corresponding results for the tangential velocity. Close to separation, the velocity profiles have a point of inflection with a reversed-flow region close to the wall. The lines of constant velocity are also steepening close to breakdown.

A very typical behavior is shown in figures 29(a) and 29(b), where the normal velocity grows very rapidly in the outer part of the boundary layer.

In figure 30, vorticity contours in the $\bar{T}$-y_1-domain are plotted for various x_1-positions starting at $x_1 = 0.3$ (fig. 30(a)) and marching back to $x_1 = 0.064$ (fig. 30(h)). The right-hand side of each figure ($\bar{T} = 1$) coincides with the numerical breakdown of the boundary-layer calculation.

It is important to notice the strong increase of maximum vorticity strengths as the leading edge is approached (decreasing x_1), as well as the increasing steepness of the contour lines at breakdown. The figures again indicate a strong vorticity ejection away from the wall.

Figure 32 is a three-dimensional plot of vorticity over the x_1-y_1-domain. A typical, strong vorticity source is observed at the wall, coinciding with the inviscid velocity peak at that position. Figure 32 displays a series of vorticity contour plots which are now given in the x_1-y_1-domain at various time-levels starting at the stagnation point and moving toward separation (see fig. 24). The spreading of the vorticity from the wall is less dramatic than that observed in the time-domain. Note the regions of negative vorticity which decrease in size when moving upstream.

The experimental pressure data again show only small deviations from (inviscid) potential theoretical calculations (ref. 3). Turbulence may be strong enough to keep the boundary layer close to the wall. A corresponding laminar separation bubble, over which transition to turbulence occurs, has also been observed in the experiment.

Case C: $\alpha = 16° + 8° \sin \omega^*T$

In the highest mean incidence case ($\alpha_0 = 16°$), the separation line (fig. 33) is located very close to the front stagnation point during the entire cycle of oscillation. The difference between the quasi-steady and unsteady ($\omega^* = 0.201$) separation position is small. A very fine mesh size of $\Delta x = 0.001$ has been used to calculate the unsteady boundary layer in these regions of extreme inviscid velocity changes. It is remarkable that now the upstream moving breakdown of the boundary layer occurs during the downstroke of the airfoil. This movement is partly caused by the specific coordinate system which is fixed to the stagnation point.

Figure 34 shows the behavior of some characteristic boundary-layer quantities plotted over the x_1-y_1-domain for a specific time ($\bar{T} = 0.486$). The changes of vorticity (fig. 34(a)) along the wall are now severe. There is, on the other hand, a steep increase of vorticity inside the boundary layer as breakdown is approached. Figure 34(b) presents the corresponding contour plots for vorticity; the vorticity created at the wall reaches the high value of 31 in this case. The outward spreading of vorticity is much steeper and stronger compared with that of the smaller incidence cases.

Figure 34(c) shows the behavior of the tangential velocity, with s-shaped profiles close to breakdown. Figure 34(d) shows the normal velocity, which reaches values of more than 250 inside the boundary layer; the other terms are of the order of 1.

Figure 35 shows the development of vorticity in the x_1-y_1-domain for different times as separation is approached. Tongues in the equal-vorticity contours are pointing away from the wall; the vorticity level is very high. Marching along the forward-moving separation between $\bar{T} = 0.366$ and $\bar{T} = 0.466$, the vorticity strength goes down and the slopes of the contour lines close to breakdown are reduced.

Figure 36 displays vorticity-distribution and plots of equal vorticity lines in the $\bar{T}$-y_1-domain. The spreading of vorticity is similar in the x_1-y_1-domain. Some oscillations in the results occurring beyond the vorticity maximum indicate that the time-step in the numerical calculation ($\Delta T = 0.01$) was too large.

In this very high incidence case ($\alpha = 16° + 8° \sin \omega T$), strong deviations of the experimental pressures from inviscid potential theory are observed (ref. 3). These deviations start very close to the leading edge and are expressed by a strong phase shift and by a reduction of the leading-edge peak of the steady and first harmonic unsteady pressures. A strong ejection of vorticity from the wall may now have overcome the effect of turbulence to shift energy toward the wall. The present results give an indication of the amount and strength of this spreading vorticity.

CONCLUSION

A finite-difference procedure has been developed for investigating dynamic stall on oscillating configurations. This procedure calculates the unsteady laminar boundary layer over a wing with a NACA 0012 airfoil section oscillating in pitch about its quarter-chord axis. Results from an unsteady panel-method are used as the outer boundary conditions, and initial conditions in both the time- and x-domains have been specified. To start the numerical calculation at the instantaneous location of the front stagnation point, a transformation of the unsteady boundary-layer equations and boundary conditions into a stagnation-point fixed frame of reference was performed.

Three incidence cases were treated in the present study: case A, $\alpha = 0° + 8° \sin \omega t$; case B, $\alpha = 8° + 8° \sin \omega t$; and case C, $\alpha = 16° + 8° \sin \omega t$. Emphasis was on determining the separation lines in the x-T-domain. The forward-moving separation occurred, with a sudden breakdown of the numerical calculation shown as a violation of the CFL condition. Characteristic boundary-layer quantities show strong variations near this breakdown. Specifically, the normal velocity inside the boundary layer shows a steep increase.

In a manner similar to that of three-dimensional steady boundary layers, where separation lines have been specified as envelopes of limiting streamlines, corresponding "limiting streamlines" in the two-dimensional x_1-$\bar{T}$-domain show the same behavior in forming an envelope. Before breakdown occurs, a considerable region of backflow develops, through which the numerical calculation continues without complications.

Investigation of the vorticity distribution in the vicinity of unsteady flow separation was emphasized in the present study. In all cases, a strong spreading of vorticity into the fluid was observed close to breakdown. The vorticity level was increased to very high values in the high mean incidence case (case C).

In case C, experimental investigations show severe deviations of the pressure distribution compared with calculated inviscid results which were not visible in the smaller incidence cases. It is assumed that if the spreading of the vorticity is strong enough to overcome the effect of turbulence, which has the tendency to keep the flow attached to the wall, a concentrated leading-edge vortex may form which is fed by the spreading vorticity developed in the laminar boundary layer. Detailed investigations have provided some insight into the mechanism of vorticity spreading and of the amount of vorticity developed in the boundary layer close to separation.

The present study deals with a weak interaction procedure: the outer boundary condition cannot adjust to the displacement effect of the boundary layer. This shortcoming could be removed by a strong interaction procedure with a recalculation of the outer boundary condition during the time-marching process.

REFERENCES

1. McCroskey, W. J.; and Philippe, J. J.: Unsteady Viscous Flow on Oscillating Airfoils. AIAA J., vol. 13, no. 1, Jan. 1975, pp. 71-79.

2. McCroskey, W. J.; McAlister, K. W.; Carr, L. W.; and Pucci, S. L.: An Experimental Study of Dynamic Stall on advanced Airfoil Sections. NASA TM-84245, vols. I, II, III (USAAVRADCOM TR-82-A-8), 1982.

3. Geissler, W.: Theoretical and Experimental Dynamic Stall Investigations on a Rotor Blade Tip. Paper presented at The Second Symposium: Numerical and Physical Aspects of Aerodynamic Flows, California State U., Long Beach, Calif., Jan. 1983 (to be published).

4. Geissler, W.: Unsteady Laminar Boundary Layer Calculations on Oscillating Configurations Including Backflow. Part I: Flat Plate, Oscillating in Its Own Plane. Nasa TM-84319, 1983.

5. Geissler, W.: Three-Dimensional Laminar Boundary Layer over a Body of Revolution at Incidence and with Separation. AIAA J., vol. 12, no. 12, Dec. 1974, pp. 1743-1745.

6. Cousteix, J.; and Houdville, R.: Singularities in Three-Dimensional Turbulent Boundary Layer Calculations and Separation Phenomena. AIAA J., vol. 19, no. 8, Aug. 1981, pp. 976-985.

7. Telionis, D. T.: Unsteady Viscous Flows. Springer Series in Computational Physics, Springer-Verlag, New York, Heidelberg, Berlin, 1981.

8. Geissler, W.: Nonlinear Unsteady Potential Flow Calculations for Three-Dimensional Oscillating Wings. AIAA J., vol. 16, no. 11, Nov. 1978, pp. 1168-1174.

9. Triebstein, H.; Destuynder, R.; and Hansen, H.: Investigation of the Unsteady Airloads on a Transport Aircraft Type Airfoil with Two Interchangeable Oscillating Trailing-Edge Flaps at Transonic Speeds and High Reynolds Numbers. Proceedings of the 13th Congress of the Aeronautical Sciences, ICAS, vol. 1, Seattle, Wash, Aug. 22-27, 1982.

10. Cebeci, T.; and Carr, L. W.: Prediction of Boundary Layer Characteristics on an Oscillating Airfoil. NASA TM-81303. (Also IUTAM Symposium: Unsteady Turbulent Shear Flows, Toulouse, France, 1981.)

11. Glauert, M. B.: The Laminar Boundary Layer on Oscillating Plates and Cylinders. J. Fluid Mech., vol. 1, 1956, pp. 97-110.

12. Rotta, J. C.: FORTRAN-4-Rechenprogramm fuer Grenzschichten bei Kompressiblen, Ebenen und Rotationssymmetrischen Stroemungen. Deutsche Luft- und Raumfahrt Forschungsbericht, DLR-FB 77-12, 1977.

13. Geissler, W.: Berechnung der Laminaren Dreidimensionalen Grenzschicht an Unsymmetrisch Umstroemten Rotationskoerpern mittels Differenzenverfahren. DFVLR-IB 251-73A19, 1973.

14. Geissler, W.: Three-Dimensional Laminar Boundary Layer over a Body of Revolution and with Separation. AIAA J., vol. 12, no. 12, Dec. 1974, pp. 1743-1745.

15. McAlister, K. W.; and Carr, L. W.: Water Tunnel Visualization of Dynamic Stall. J. Fluids Eng., vol. 101, Sept. 1979.

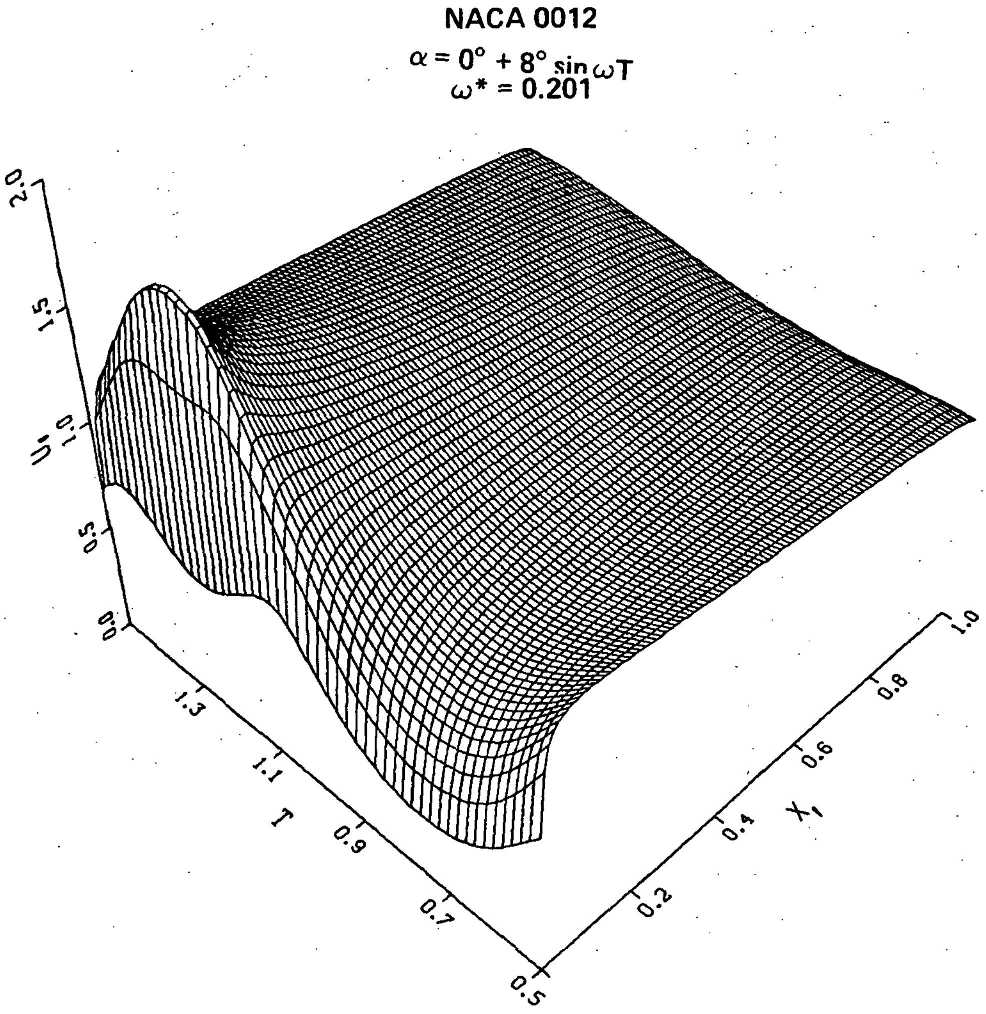

Figure 1.- Inviscid velocity distribution (panel-method) over a period of oscillation referred to the moving-stagnation-point coordinate system. $\bar{T} = 0.5$: $\alpha = 0°$, $\bar{T} = 0.75$: $\alpha = -8°$, $\bar{T} = 1$: $\alpha = 0°$, $\bar{T} = 1.25$: $\alpha = 8°$, $\bar{T} = 1.5$: $\alpha = 0°$.

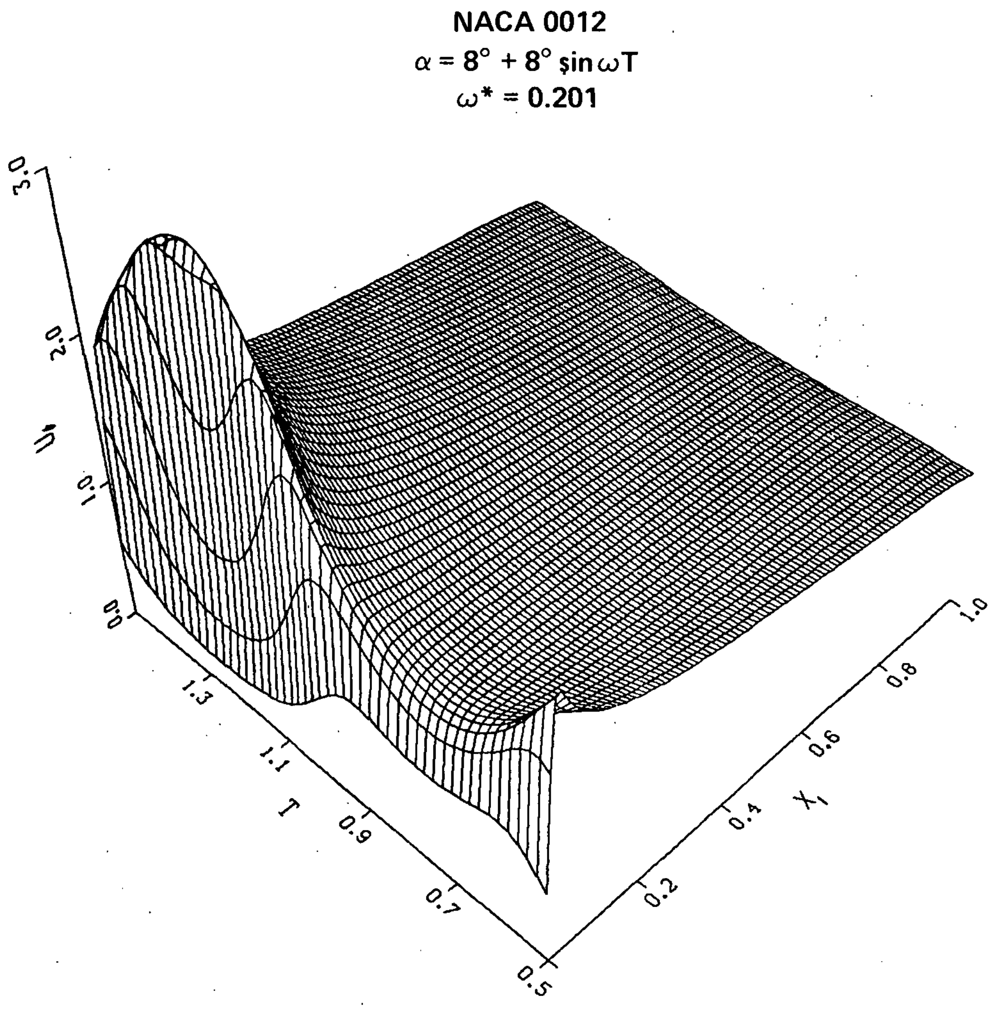

Figure 2.- Inviscid velocity distribution (panel-method) over a period of oscillation referred to the moving-stagnation-point coordinate system. $\bar{T} = 0.5$: $\alpha = 8°$, $\bar{T} = 0.75$: $\alpha = 0°$, $\bar{T} = 1$: $\alpha = 8°$, $\bar{T} = 1.25$: $\alpha = 16°$, $\bar{T} = 1.5$: $\alpha = 8°$.

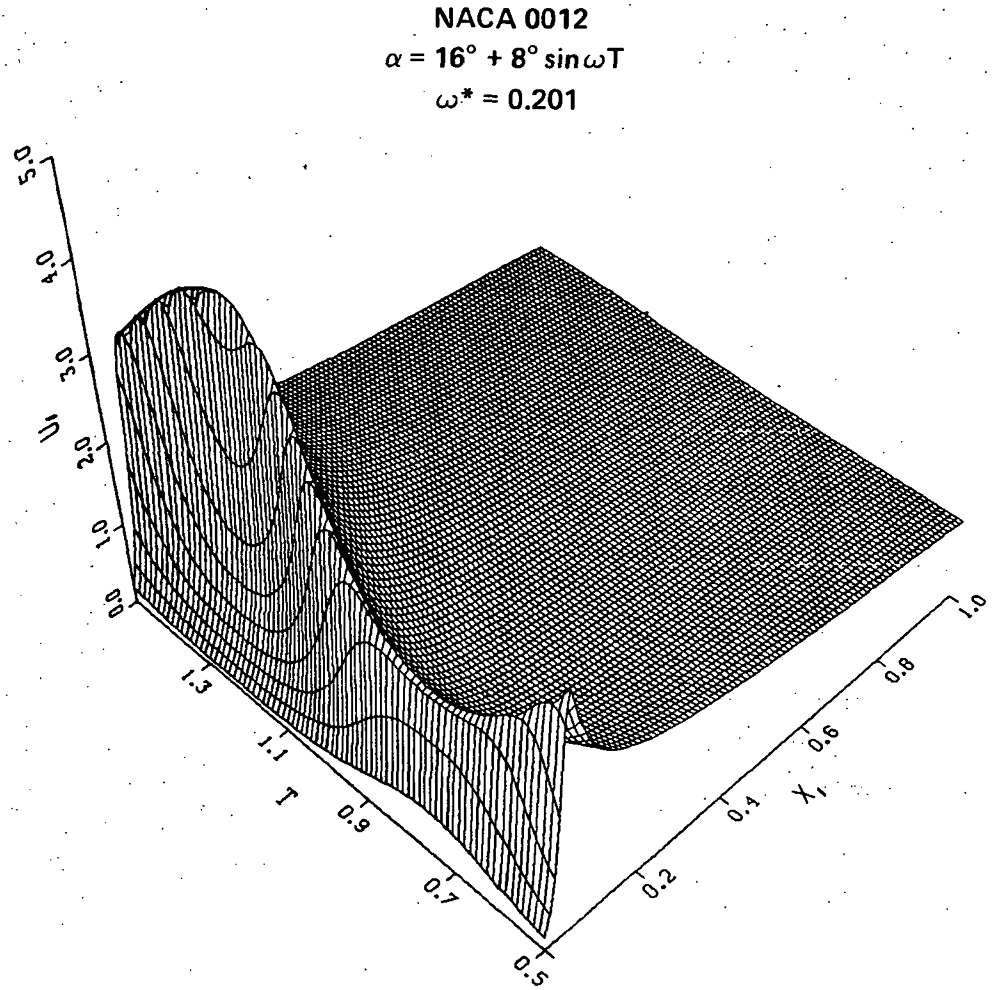

Figure 3.- Inviscid velocity distribution (panel-method) over a period of oscillation referred to the moving-stagnation-point coordinate system. $\bar{T} = 0.5$: $\alpha = 16°$, $\bar{T} = 0.75$: $\alpha = 8°$, $\bar{T} = 1$: $\alpha = 16°$, $\bar{T} = 1.25$: $\alpha = 24°$, $\bar{T} = 1.5$: $\alpha = 16°$.

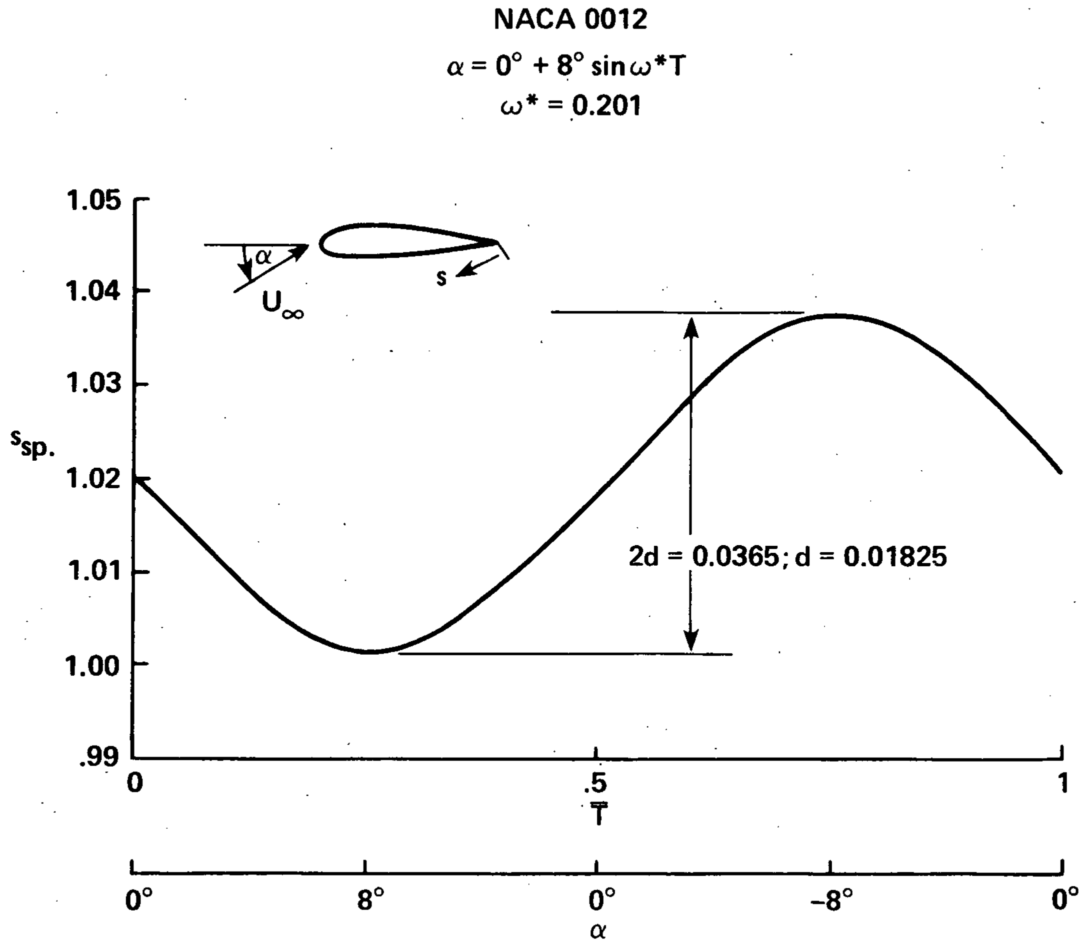

Figure 4.- Displacement of stagnation point: zero-mean incidence case.

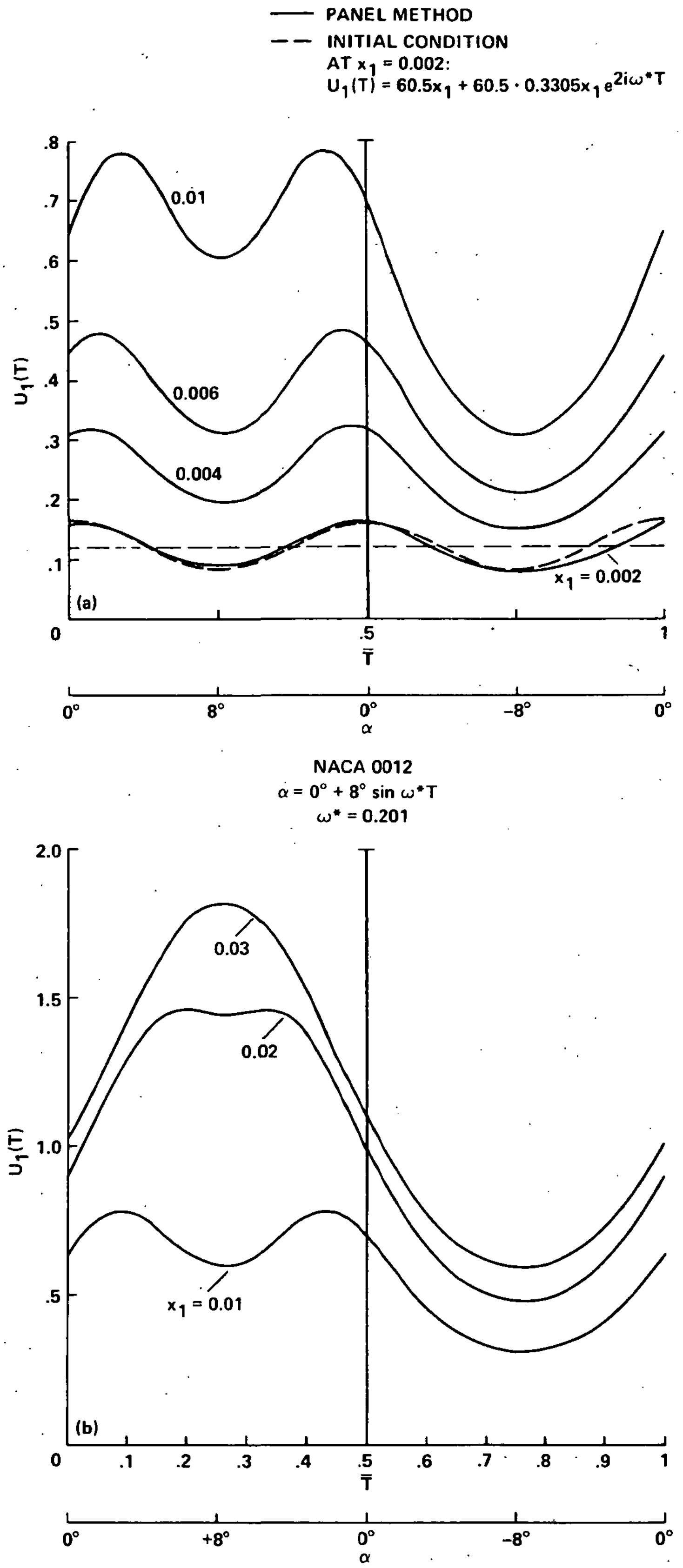

Figure 5.- Inviscid velocity distribution, harmonic fit for initial conditions: zero-mean incidence case.

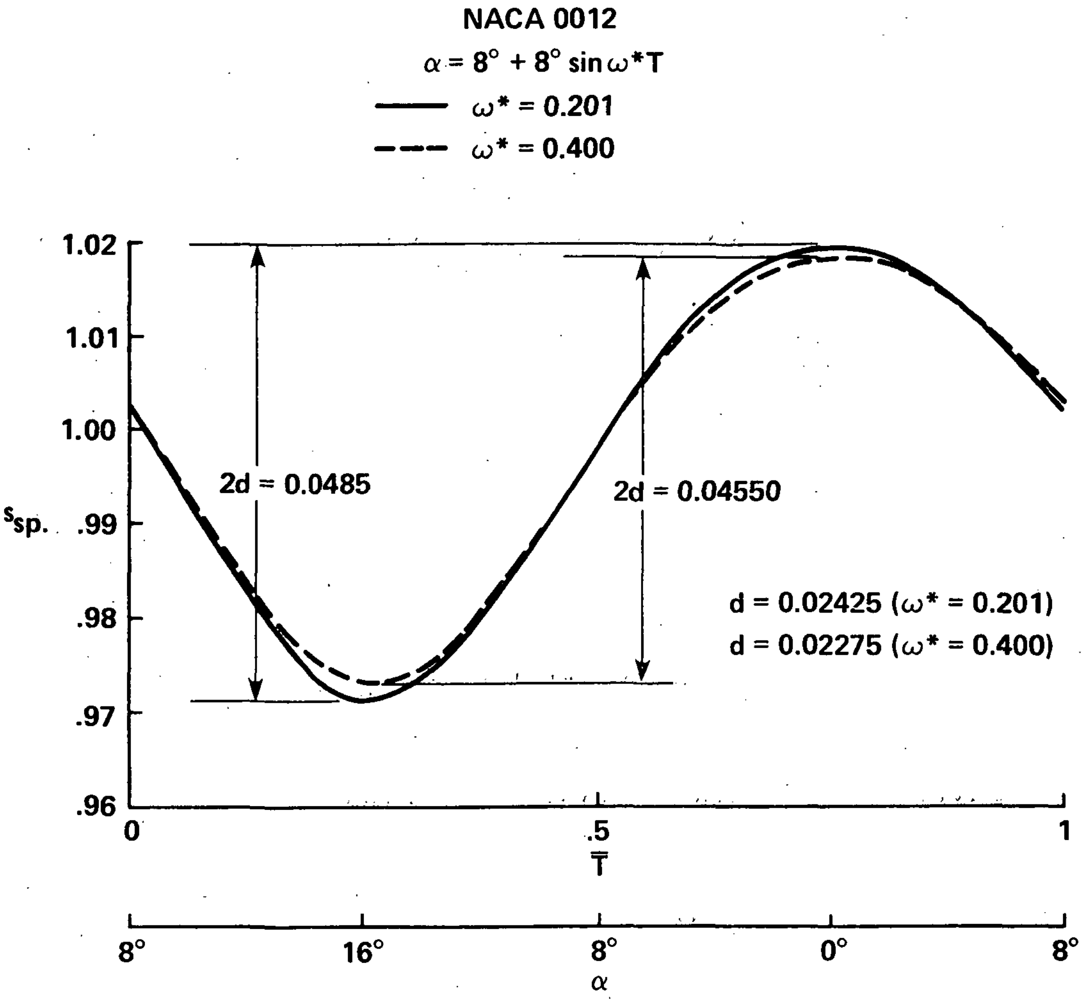

Figure 6.- Displacement of stagnation point: case A, $\alpha_0 = 0°$.

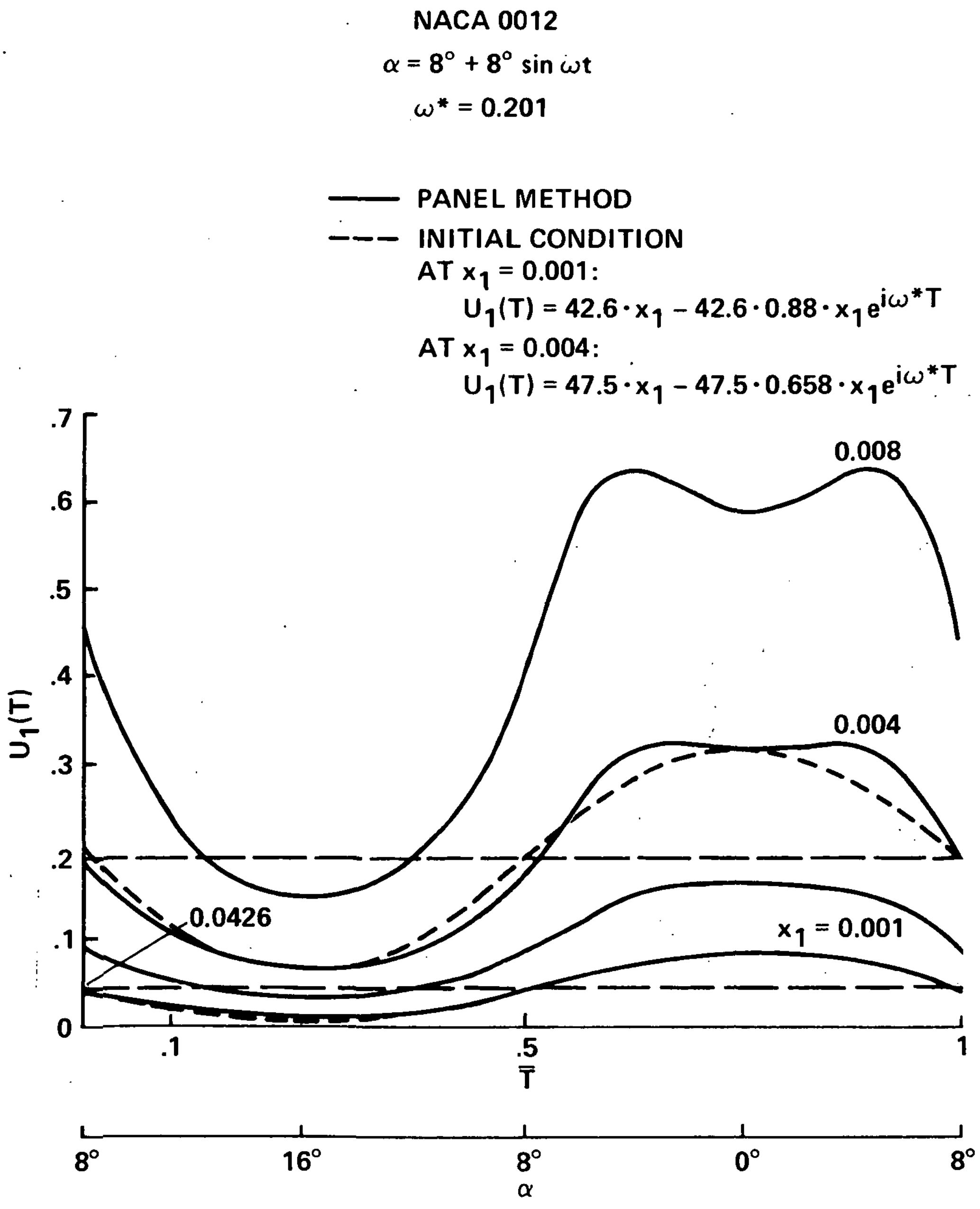

Figure 7.- Inviscid velocity distribution, harmonic fit for initial conditions: case B, $\alpha_0 = 8^\circ$.

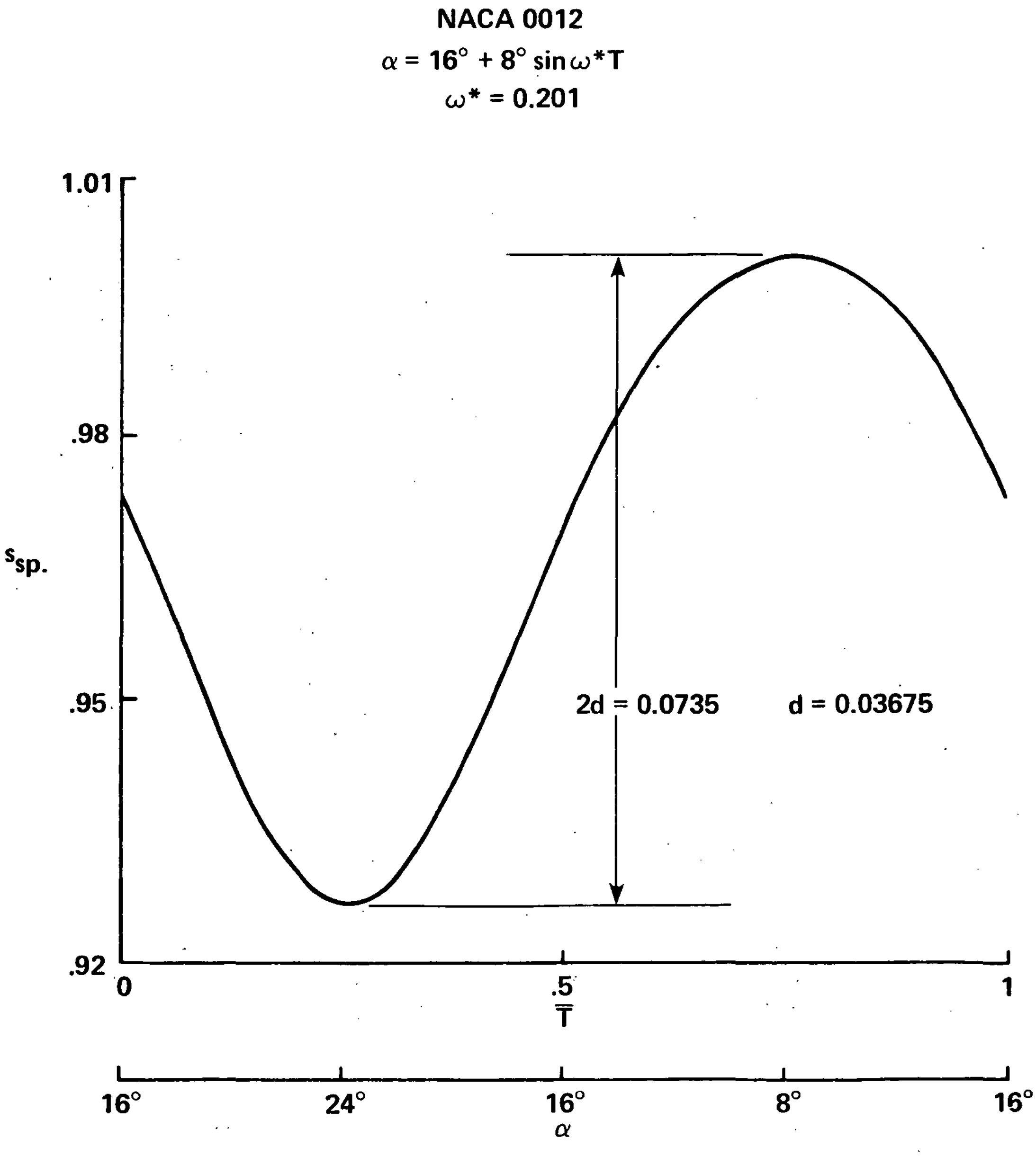

Figure 8.- Displacement of stagnation point: case C, $\alpha_0 = 16°$.

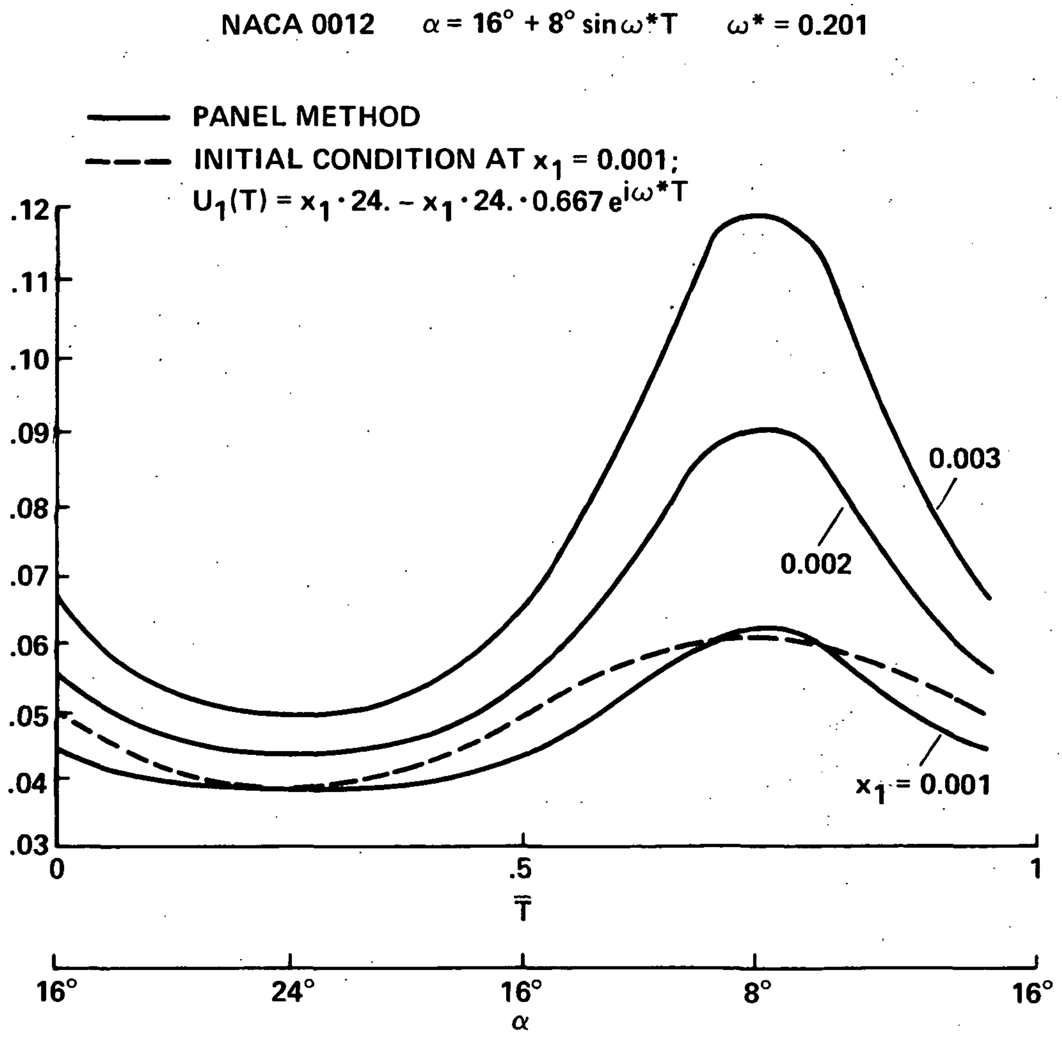

Figure 9.- Inviscid velocity distribution, harmonic fit for initial conditions: case C, $\alpha_0 = 16°$.

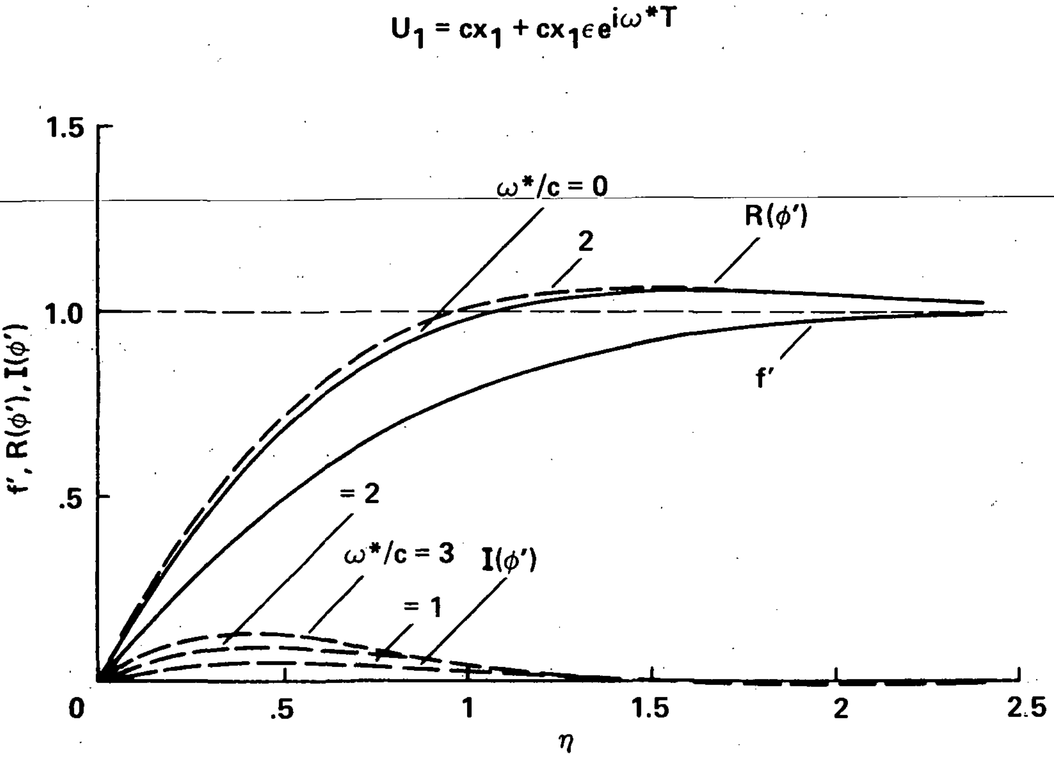

Figure 10.- Unsteady initial conditions.

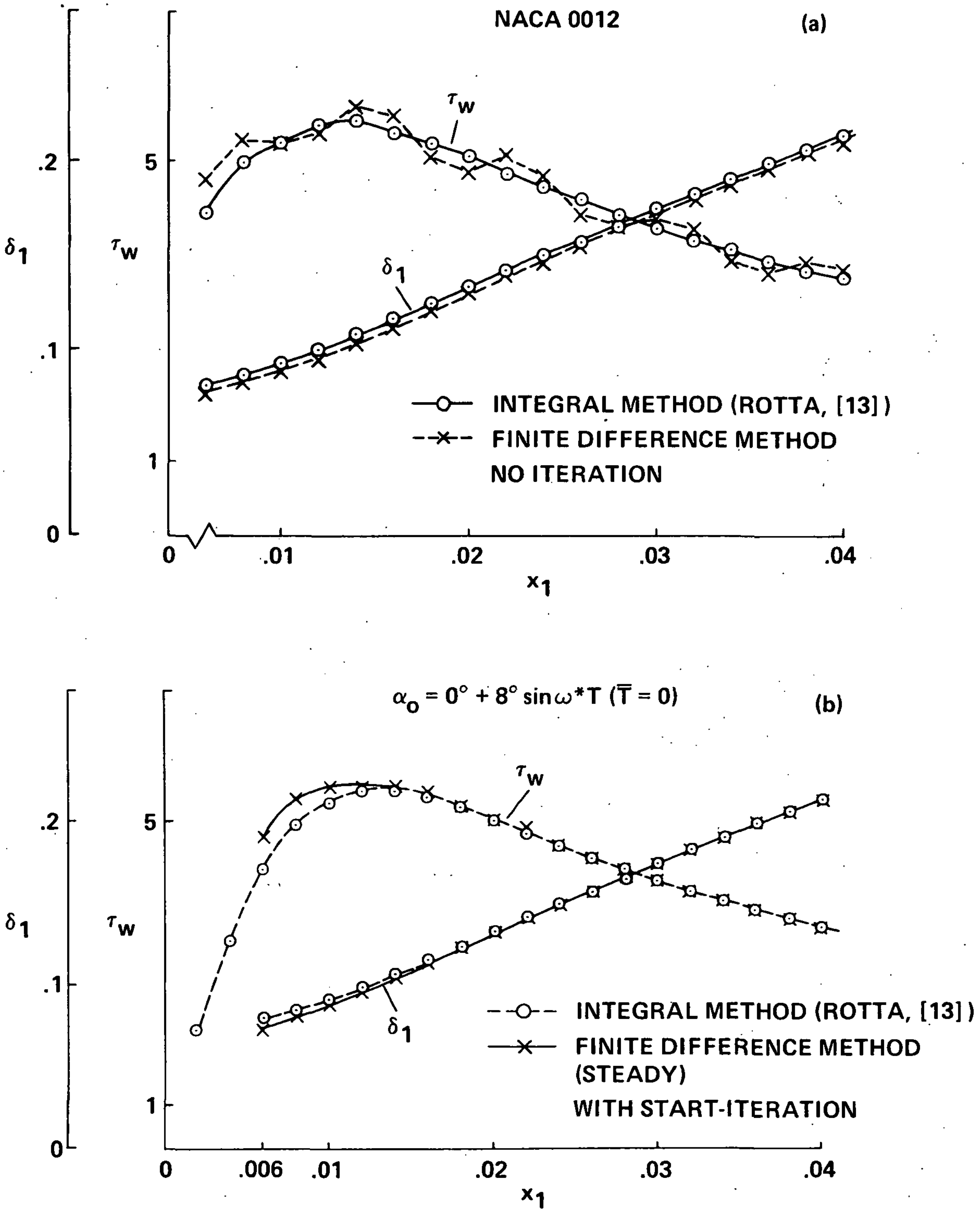

Figure 11.- Steady initial conditions.

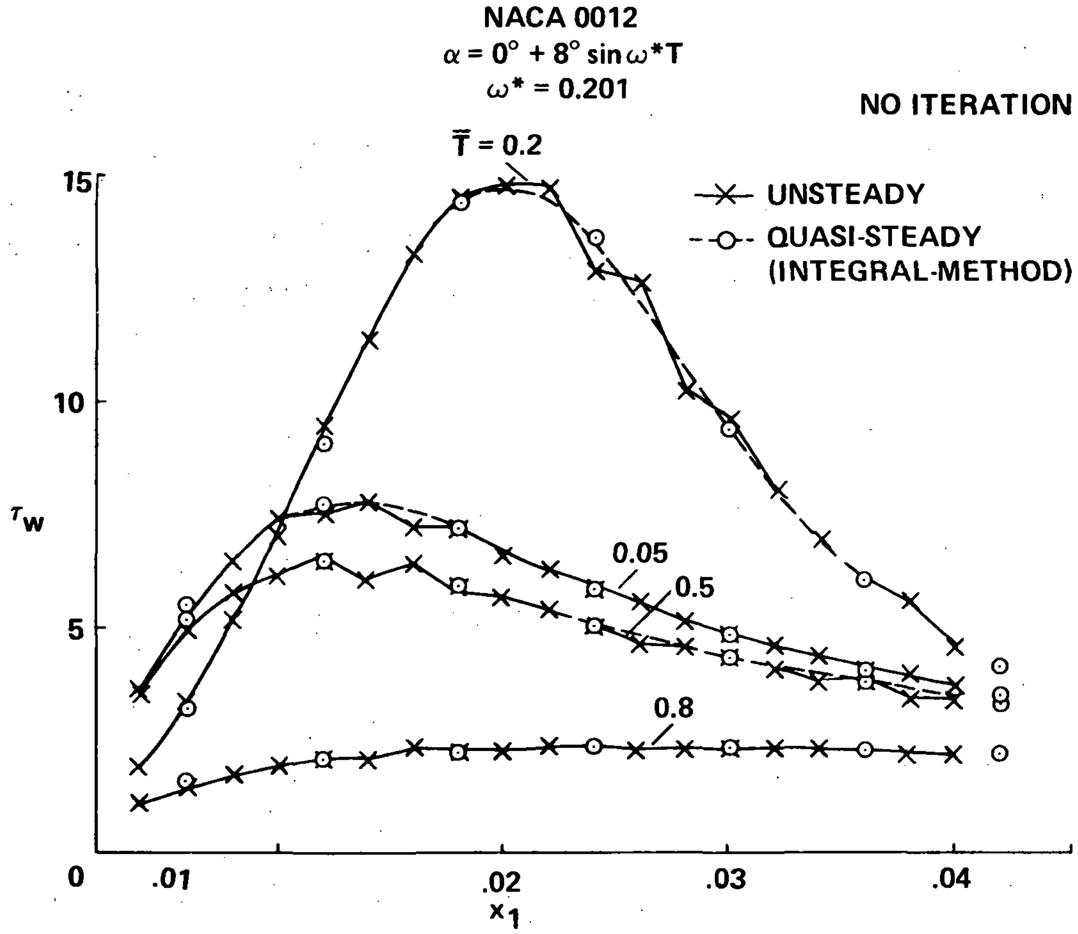

Figure 12.- Development of wall shear-stress with distance x_1 from the stagnation point, comparison with integral method: case A, $\alpha_0 = 0°$.

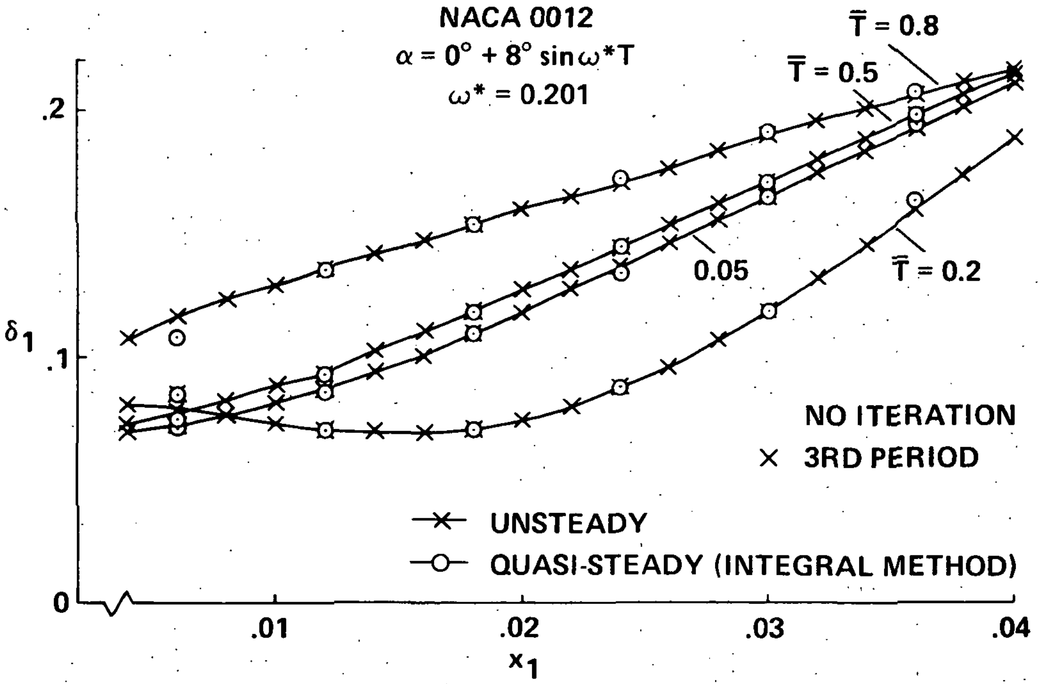

Figure 13.- Development of boundary-layer displacement thickness with distance x_1 from the stagnation point, comparison with integral method: case A, $\alpha_0 = 0°$.

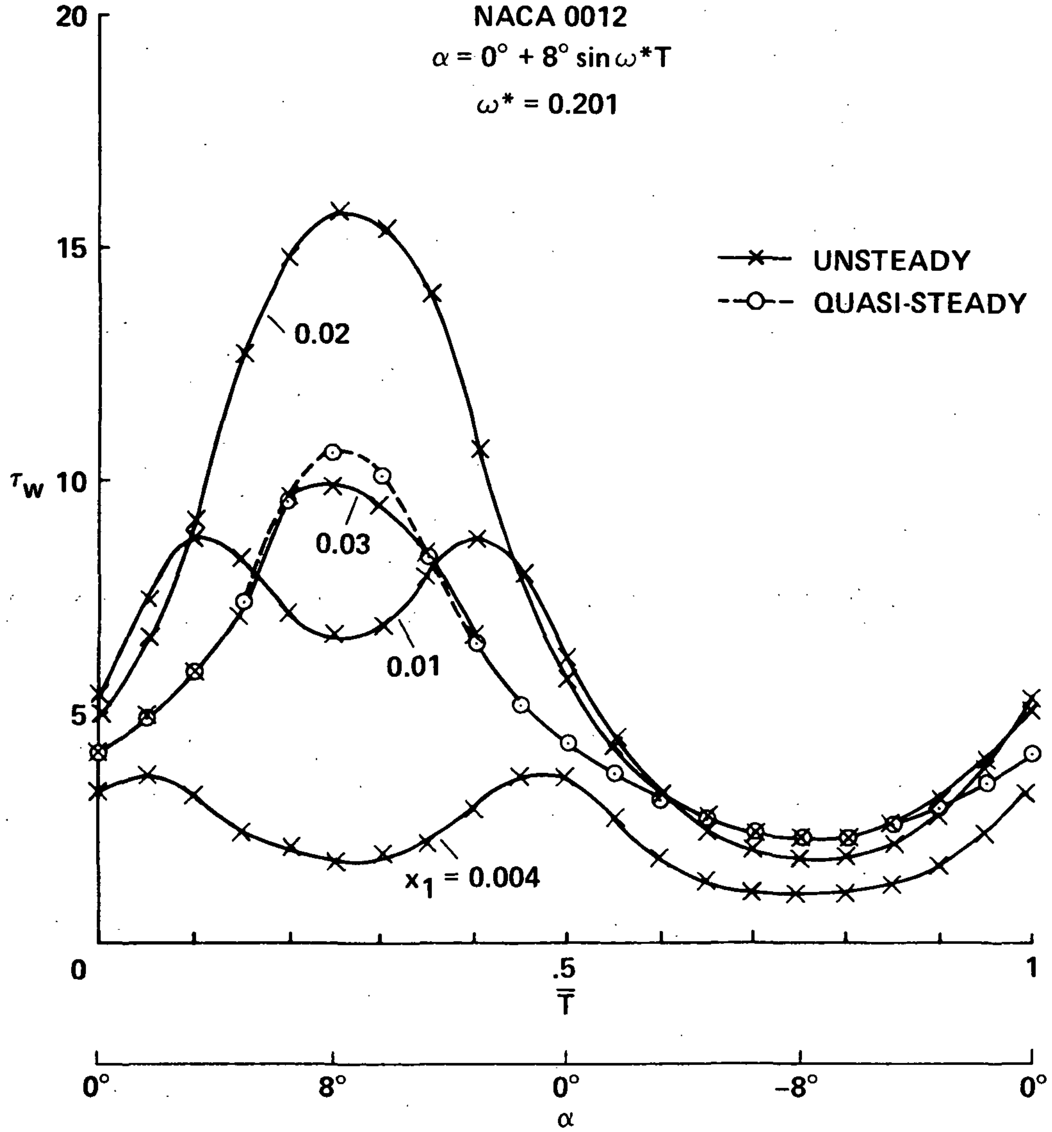

Figure 14.- Development of wall shear-stress over a period of oscillation.

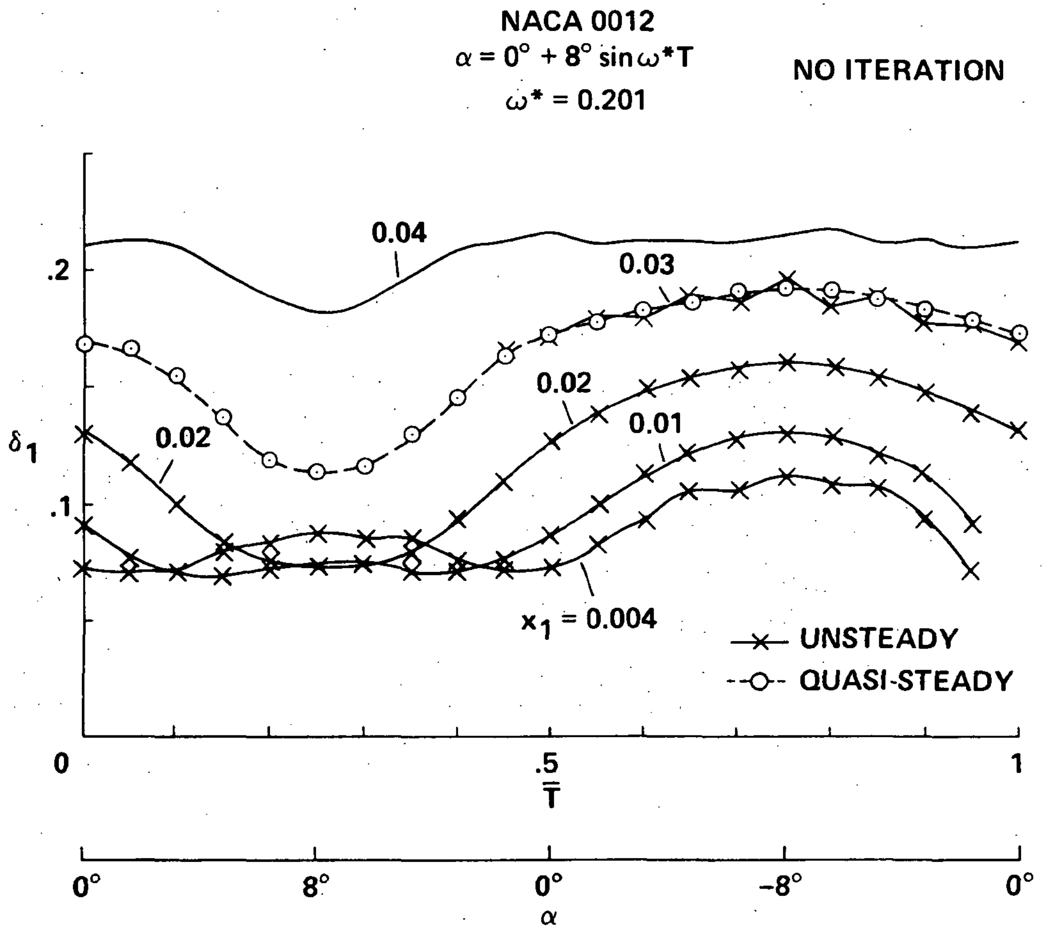

Figure 15.- Development of boundary-layer displacement thickness over a period of oscillation.

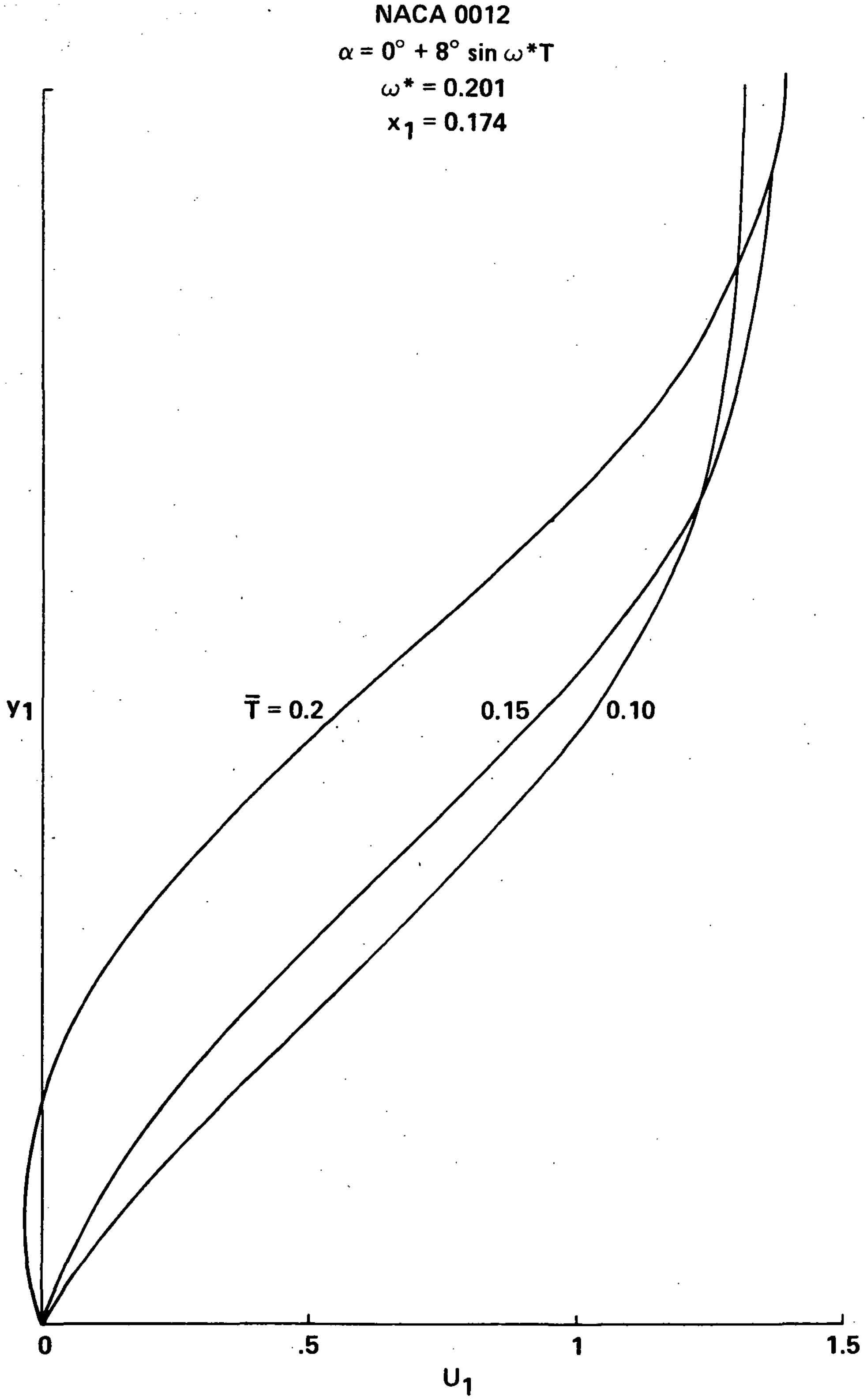

Figure 16.- Unsteady velocity profiles with backflow: case A, $\alpha_0 = 0°$.

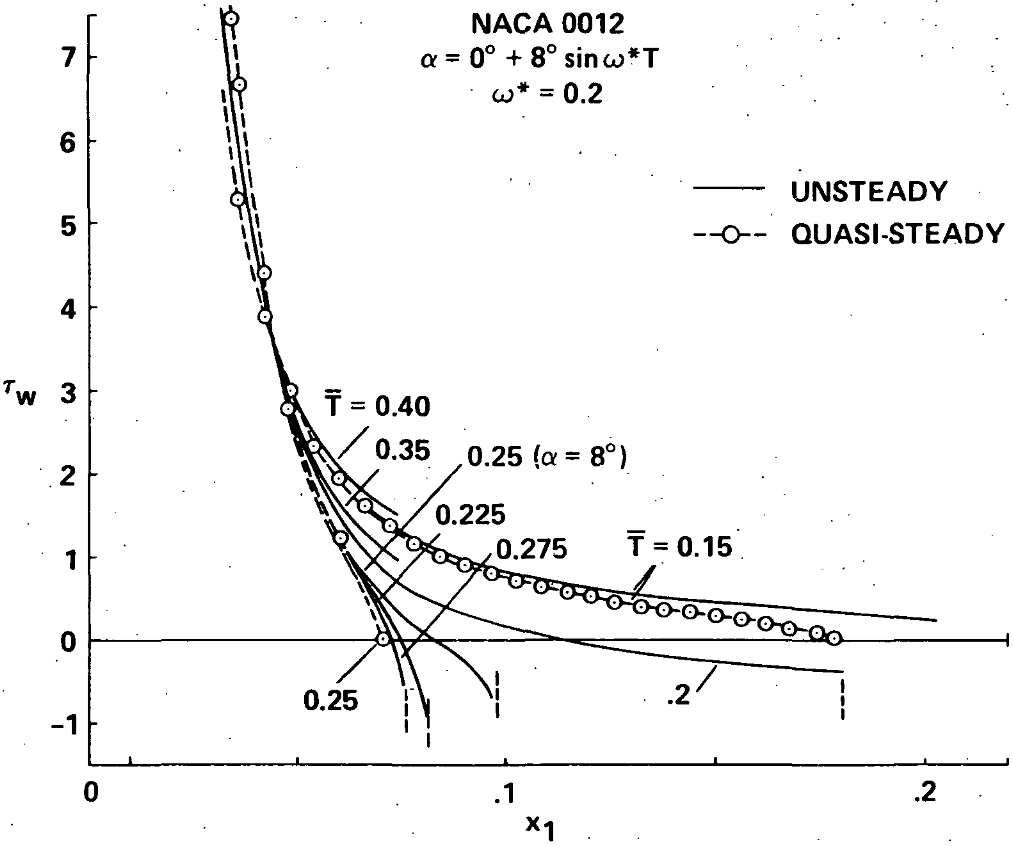

Figure 17.- Development of wall shear-stress close to unsteady separation; comparison with quasi-steady results.

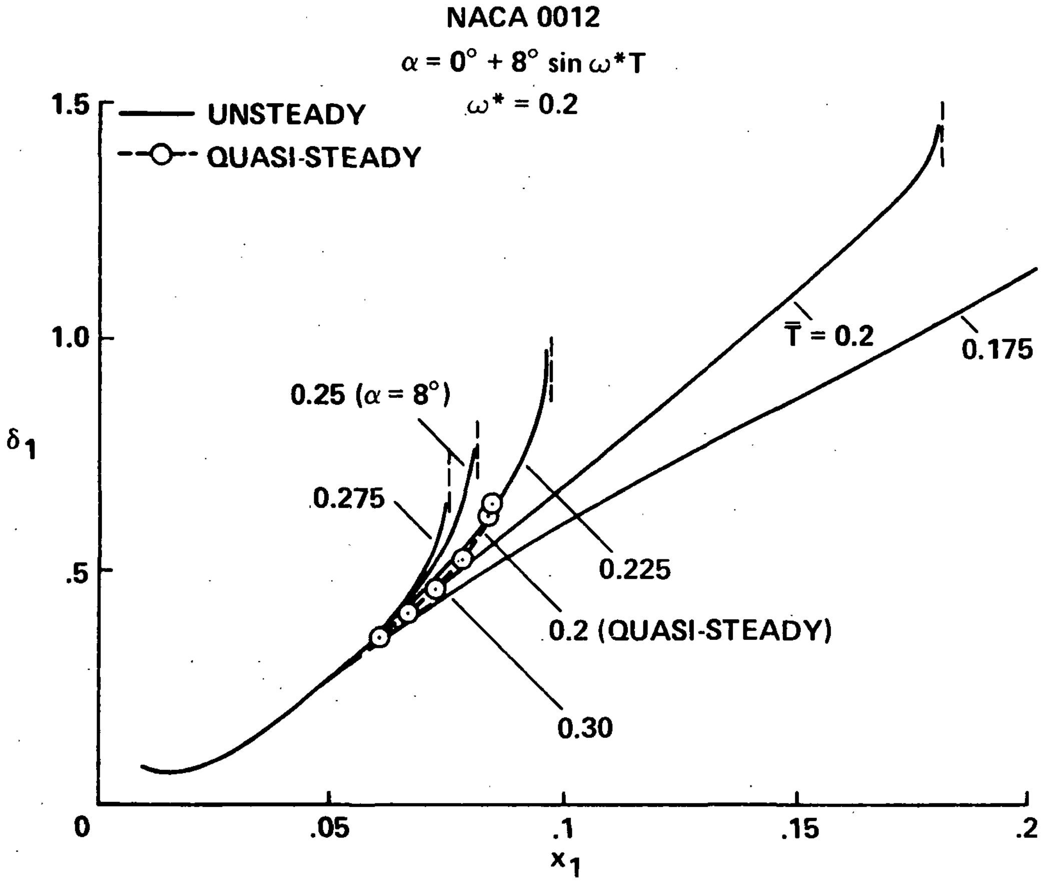

Figure 18.- Development of boundary-layer displacement thickness close to unsteady separation; comparison with quasi-steady results.

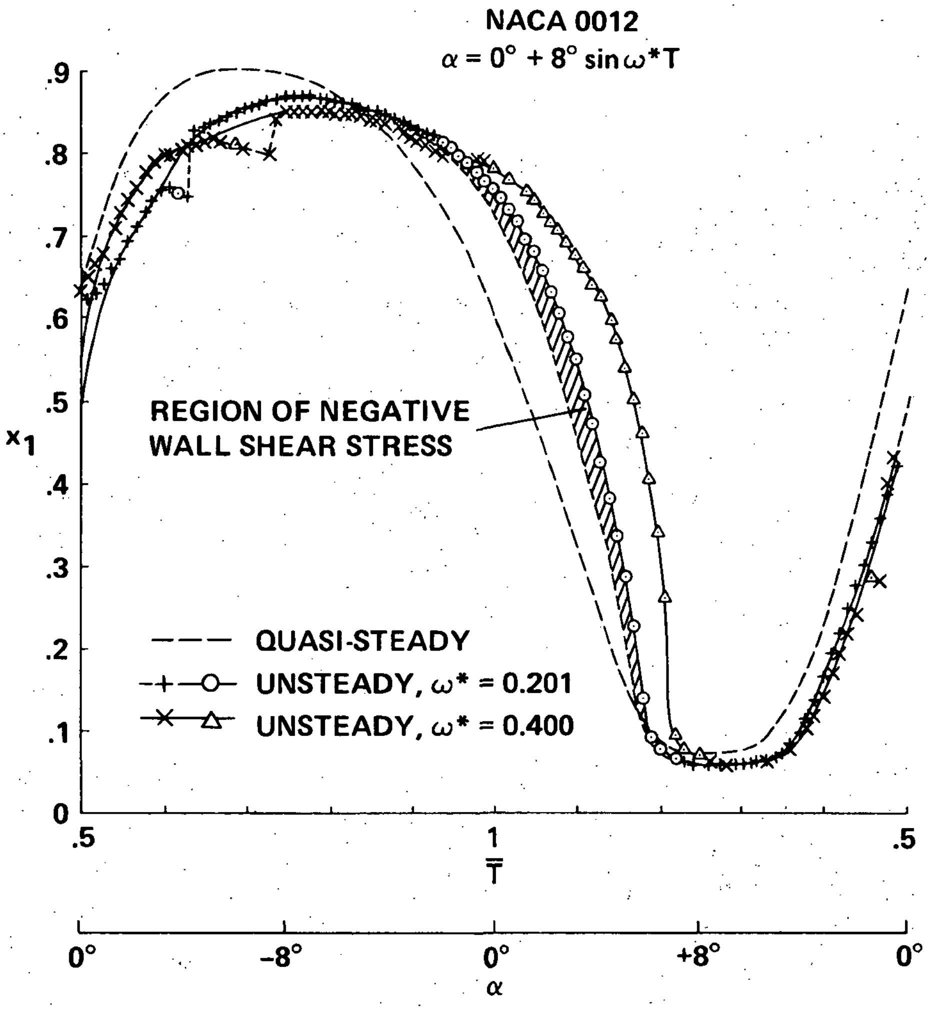

Figure 19.- Quasi-steady and unsteady separation lines over a period of oscillation: case A, $\alpha_0 = 0°$.

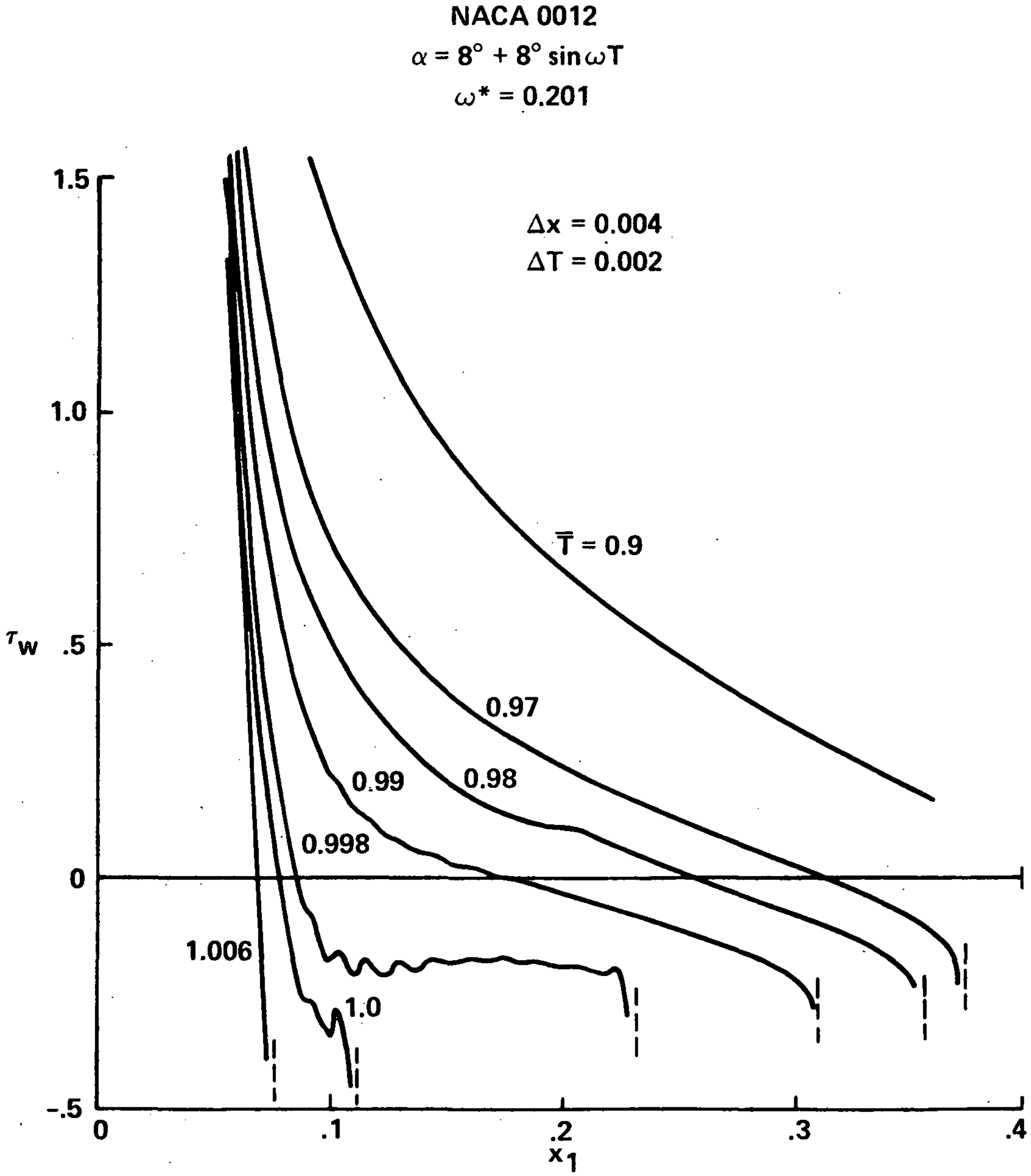

Figure 20.- Development of wall shear-stress close to separation: case B, $\alpha_0 = 8°$.

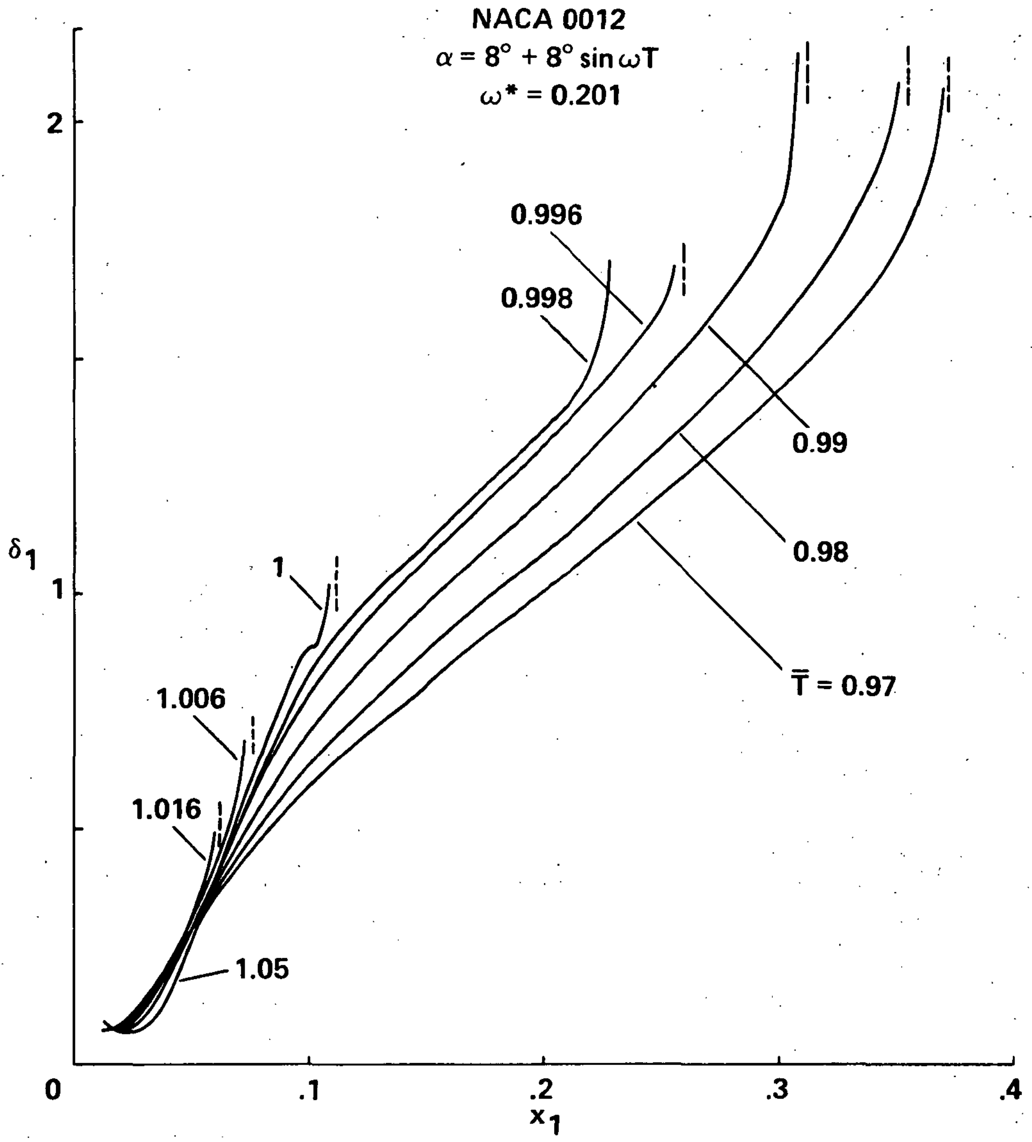

Figure 21.- Development of boundary-layer displacement thickness close to separation: case B, $\alpha_0 = 8°$.

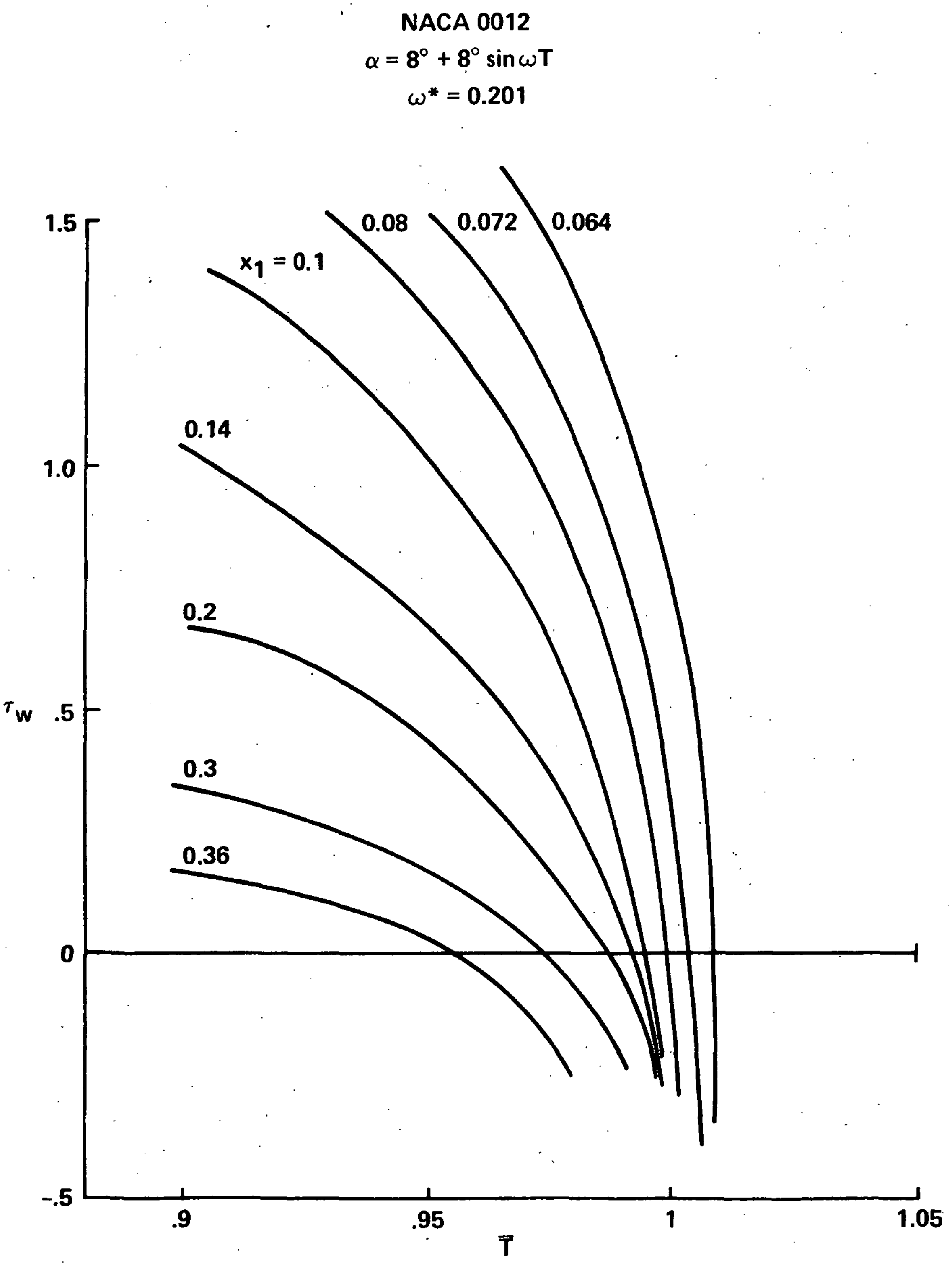

Figure 22.- Behavior of wall shear-stress over time close to separation.

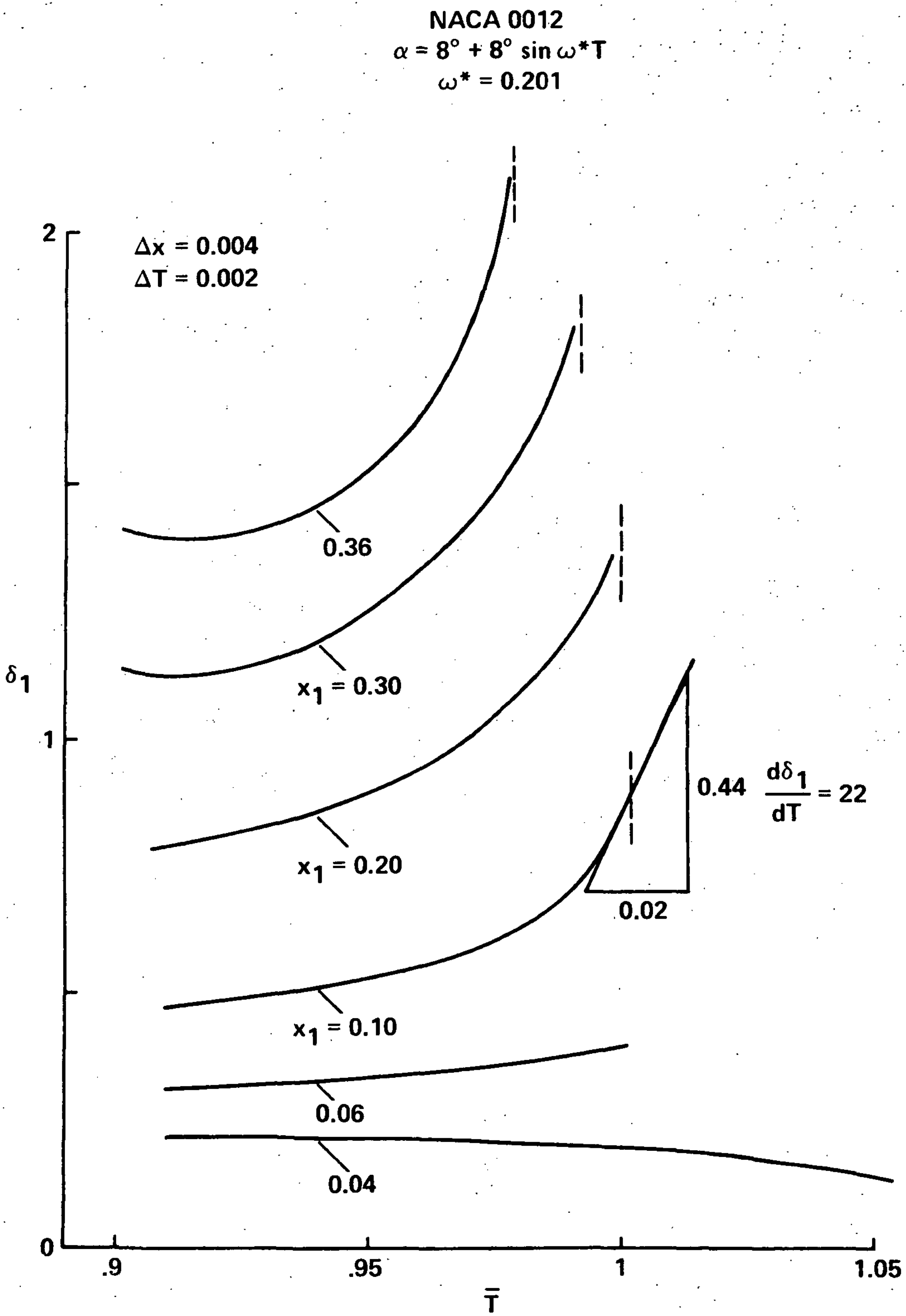

Figure 23.- Behavior of boundary-layer displacement thickness over time close to separation.

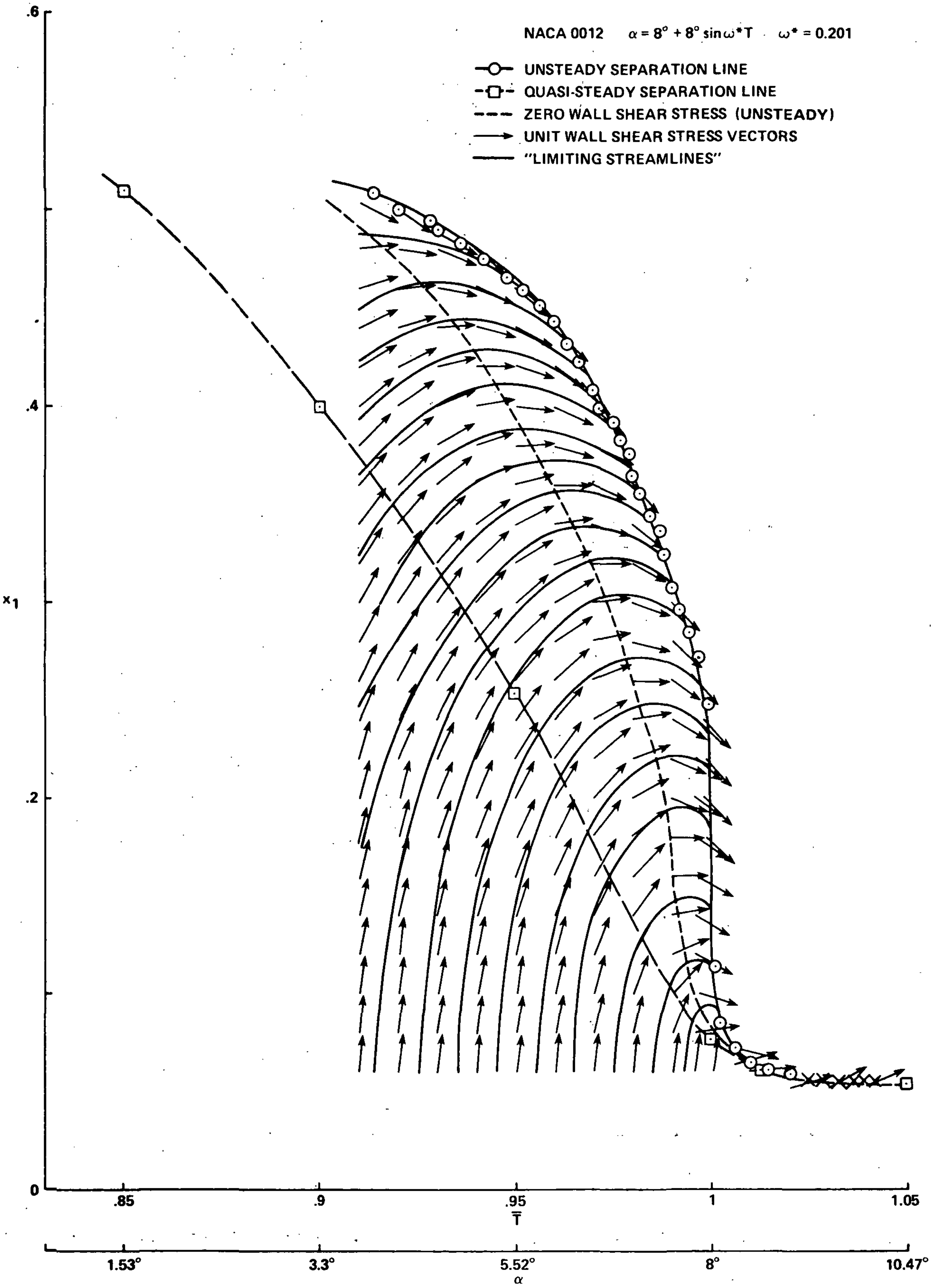

Figure 24.- Unit vectors of the wall shear-stress, "limiting streamlines," close to separation.

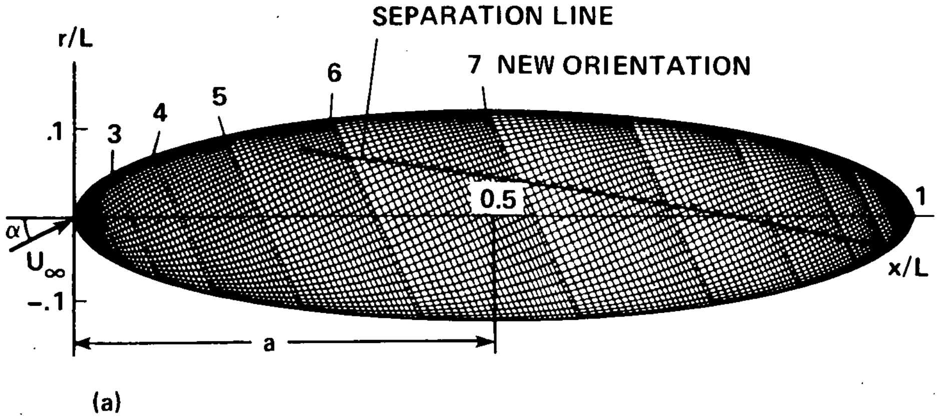

STREAMLINE NET WITH SEPARATION LINE

a/b = 4; α = 15°

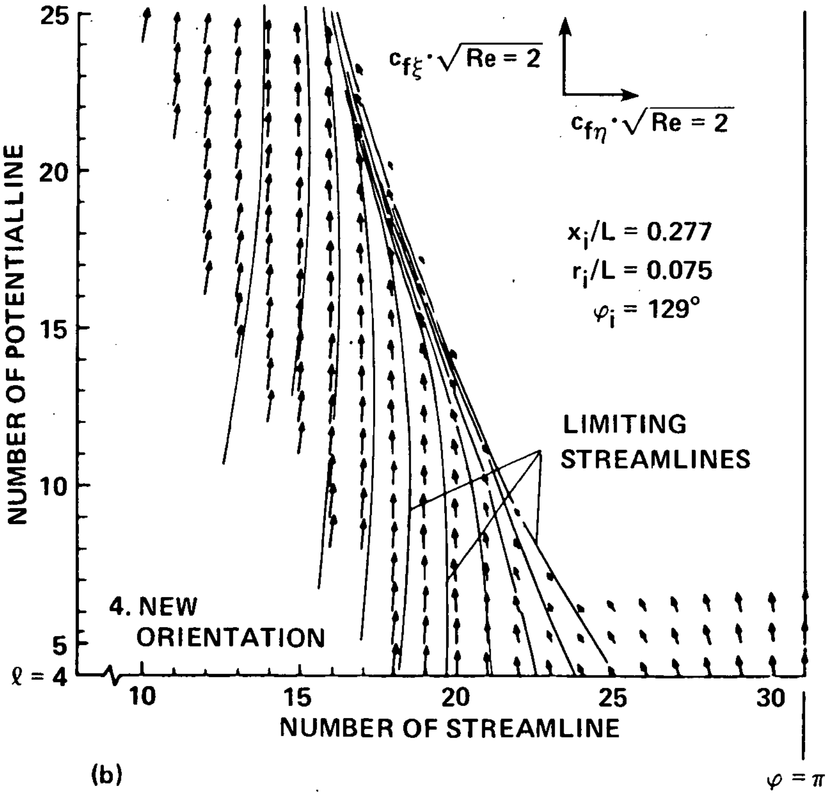

VECTORS OF WALL SHEARING STRESS AND LIMITING STREAMLINES

a/b = 6; α = 10°

Figure 25.- Three-dimensional boundary-layer calculations on a spheroid.

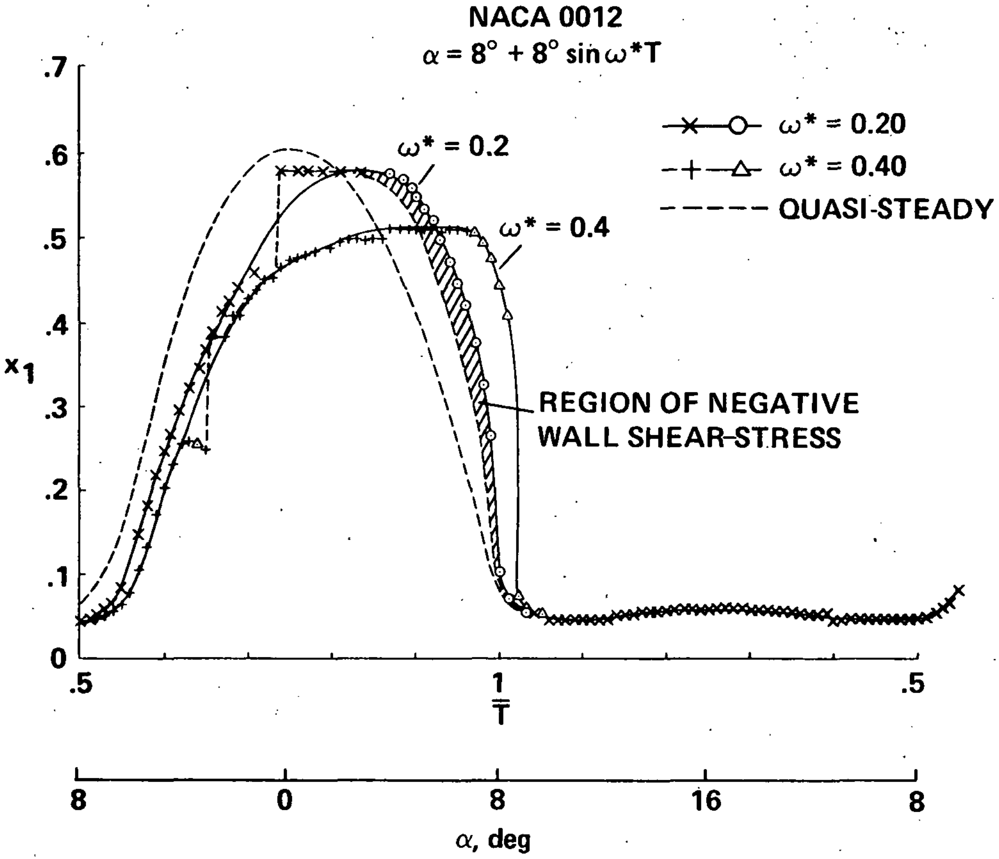

Figure 26.- Quasi-steady and unsteady separation lines over a period of oscillation: case B, $\alpha_0 = 8°$.

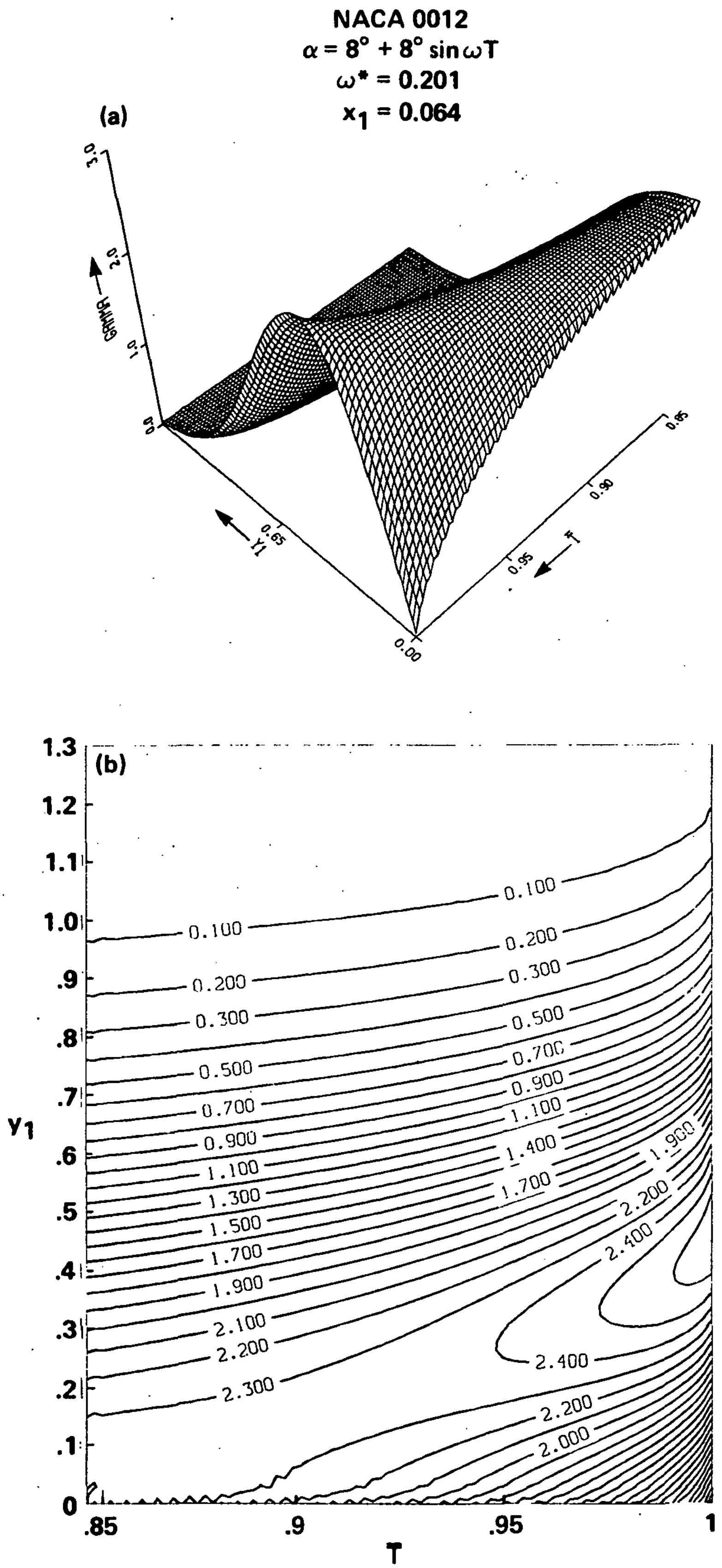

Figure 27.- Vorticity distribution and vorticity contours with respect to time, close to separation. (a) Three-dimensional plot; (b) Contour plot.

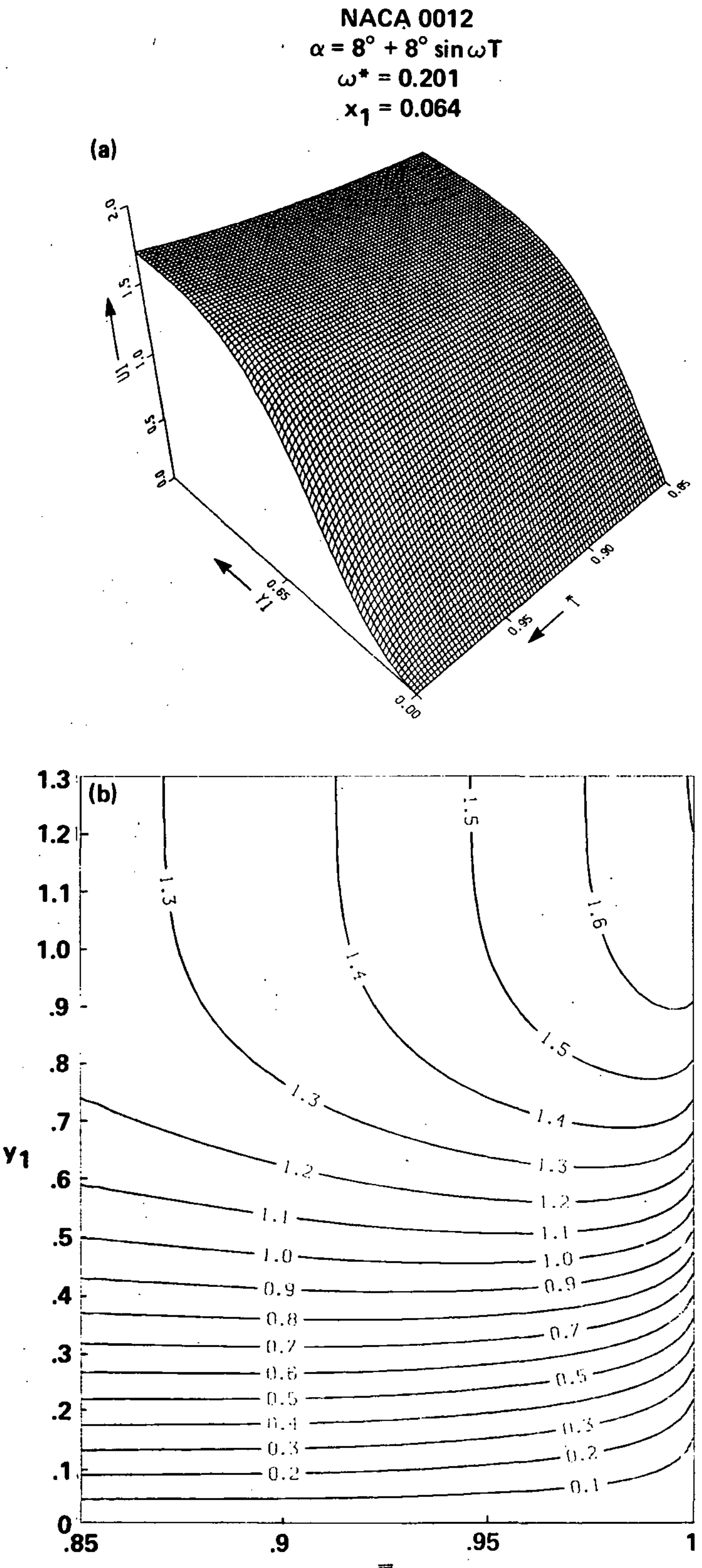

Figure 28.- Velocity profiles and velocity contours with respect to time, close to separation.

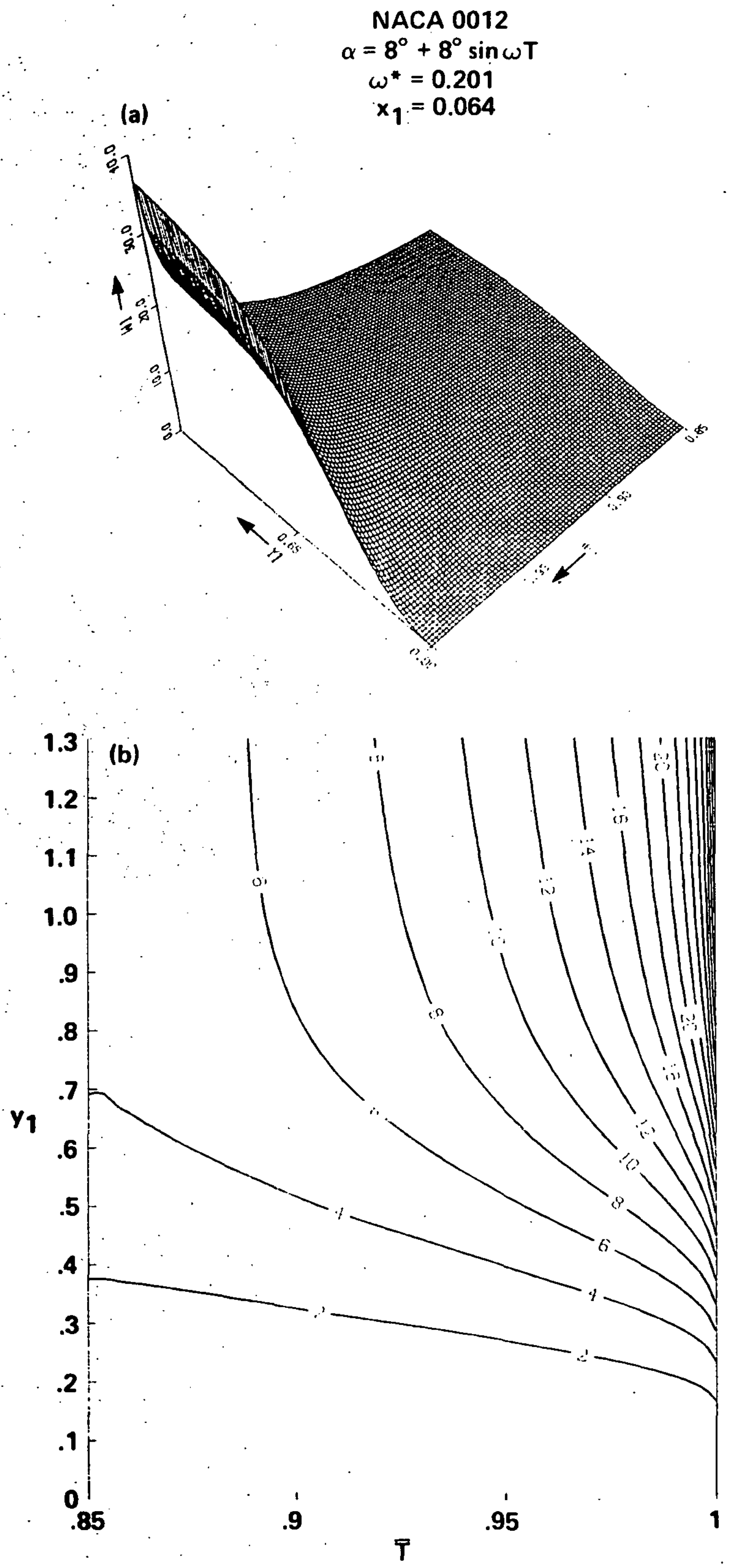

Figure 29.- Normal velocities and normal velocity contours with respect to time, close to separation.

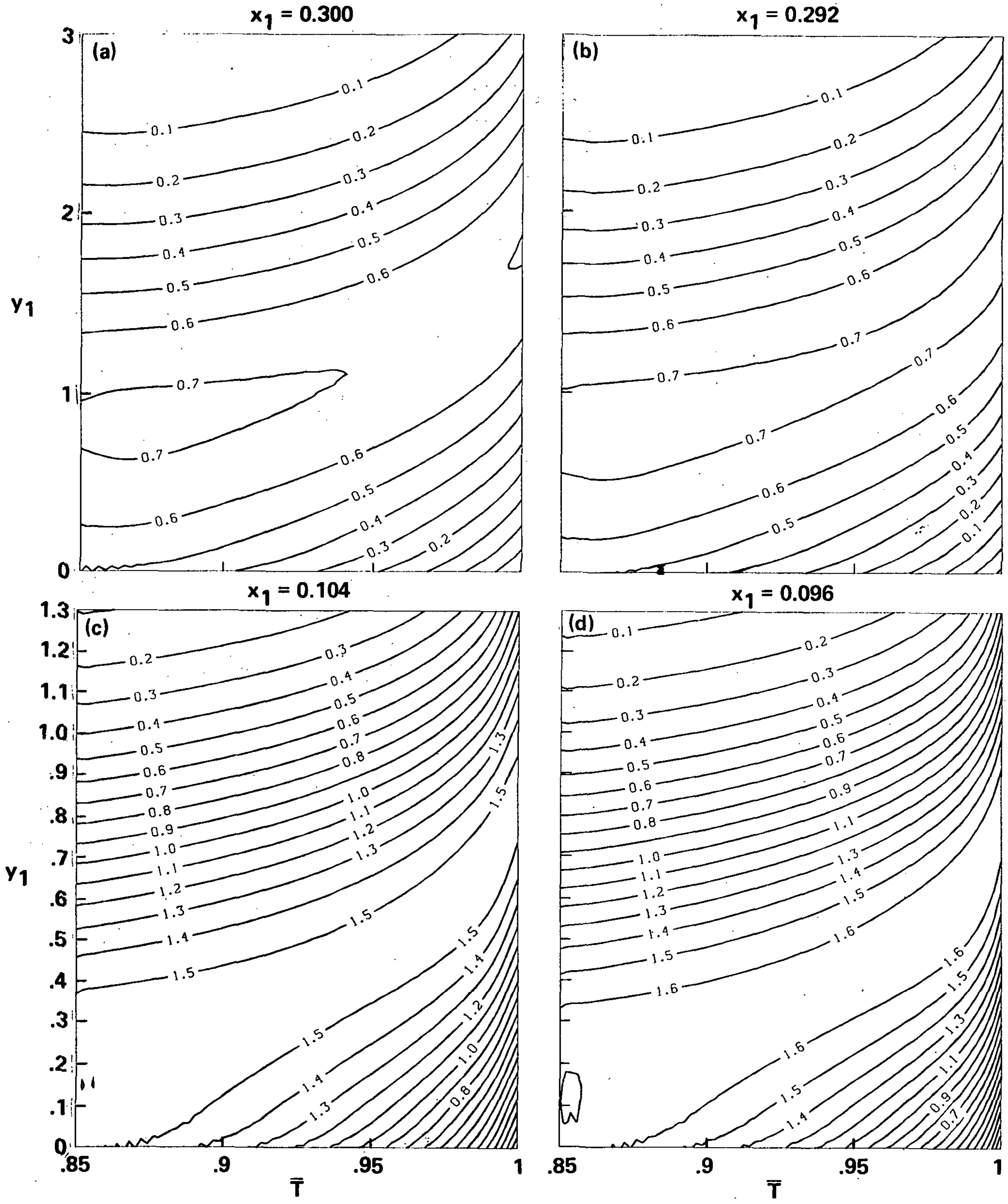

Figure 30.- Vorticity contours close to separation: case B, $\alpha_0 = 8°$ ($\omega^* = 0.2$).

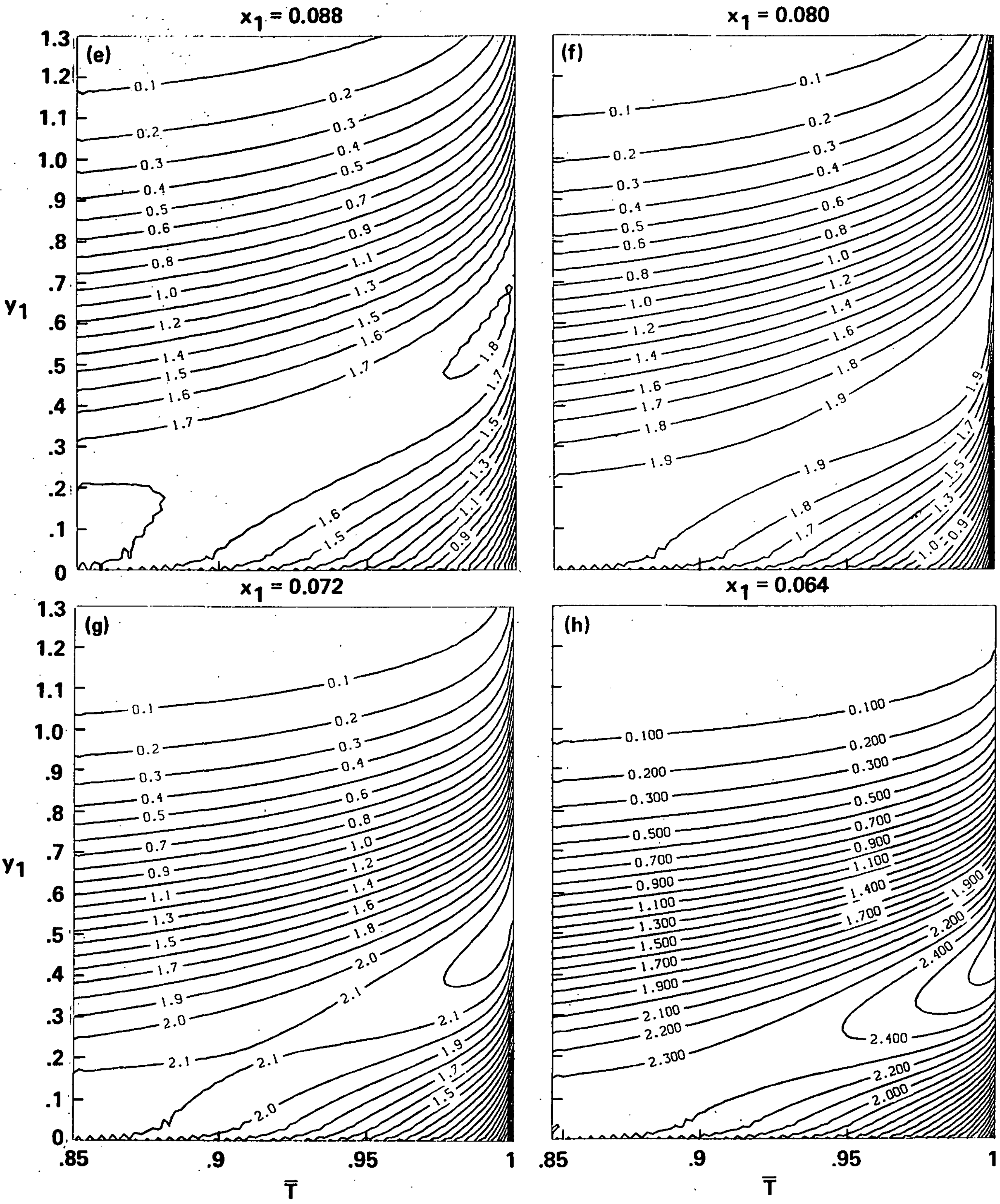

Figure 30. - Concluded

NACA 0012

$\alpha = 8^\circ + 8^\circ \sin \omega T$

$\omega^* = 0.201$

$\bar{T} = 0.996$

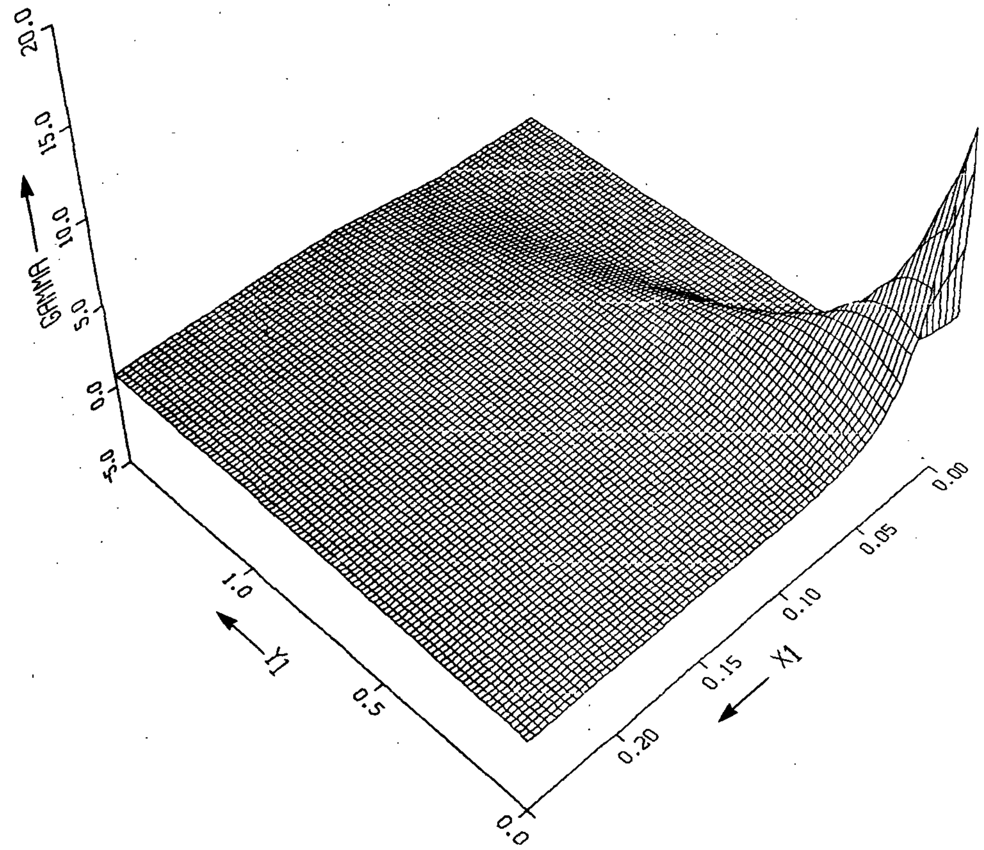

Figure 31. - Vorticity distribution with respect to x_1.

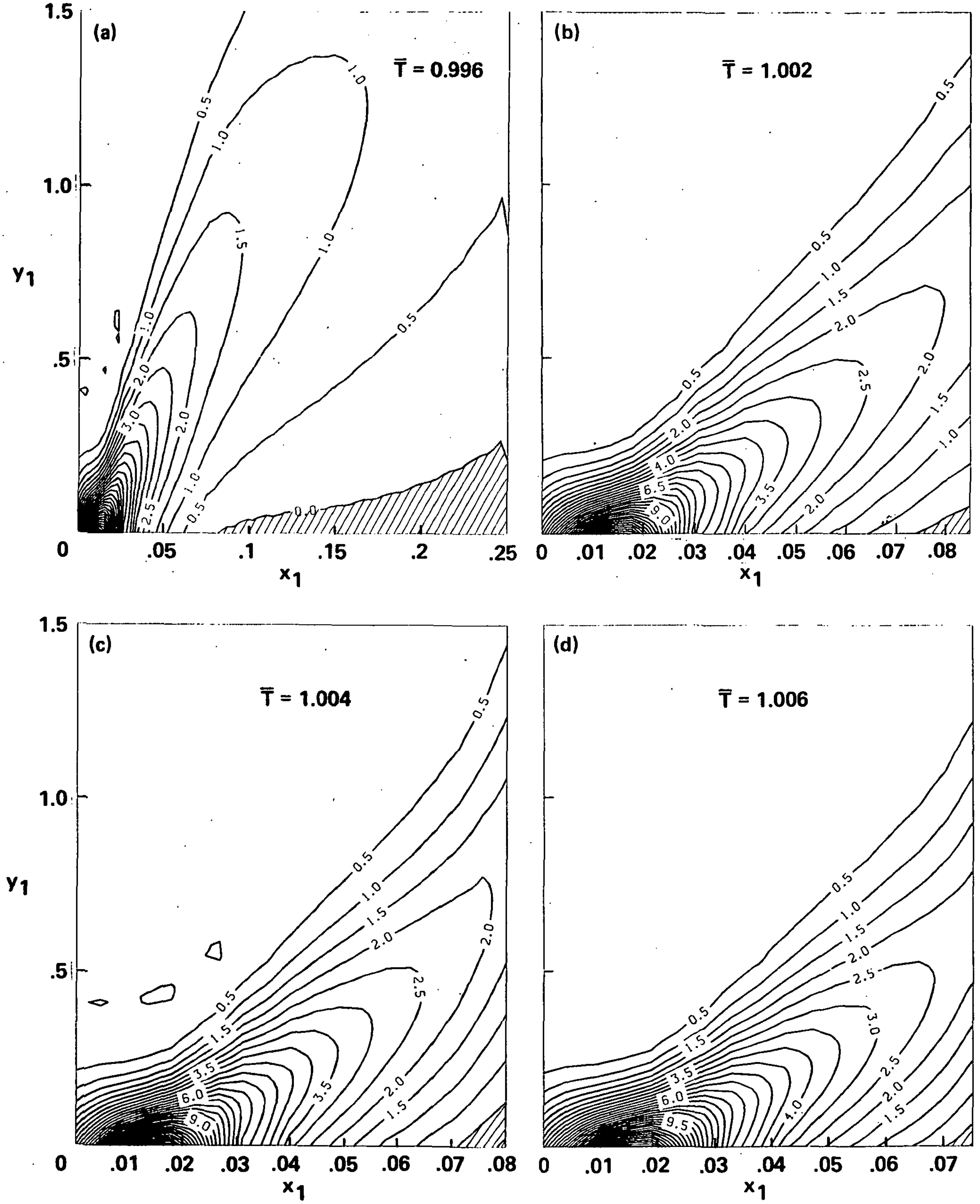

Figure 32. - Vorticity contours with respect to x_1: case B, $\alpha_0 = 8°$ ($\omega^* = 0.2$).

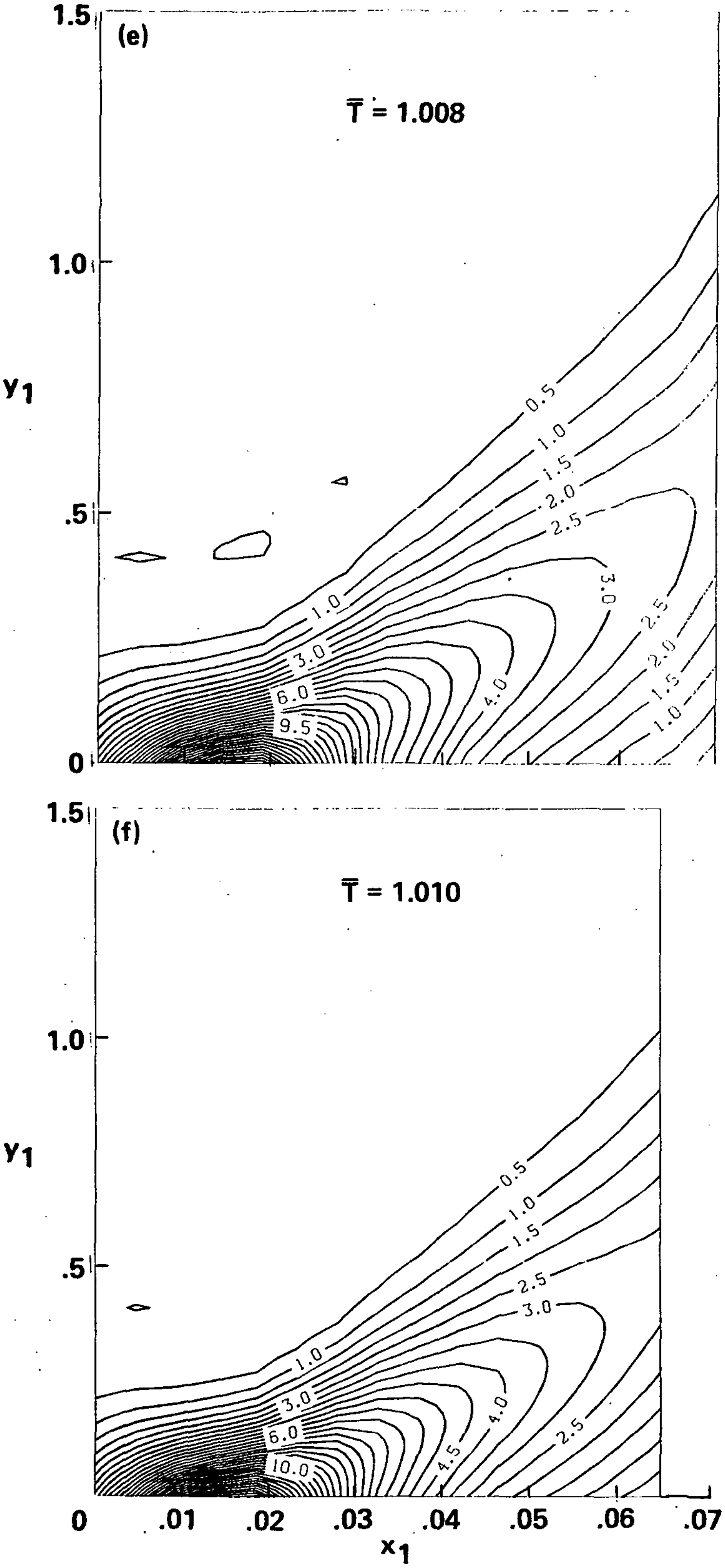

Figure 32. - Concluded

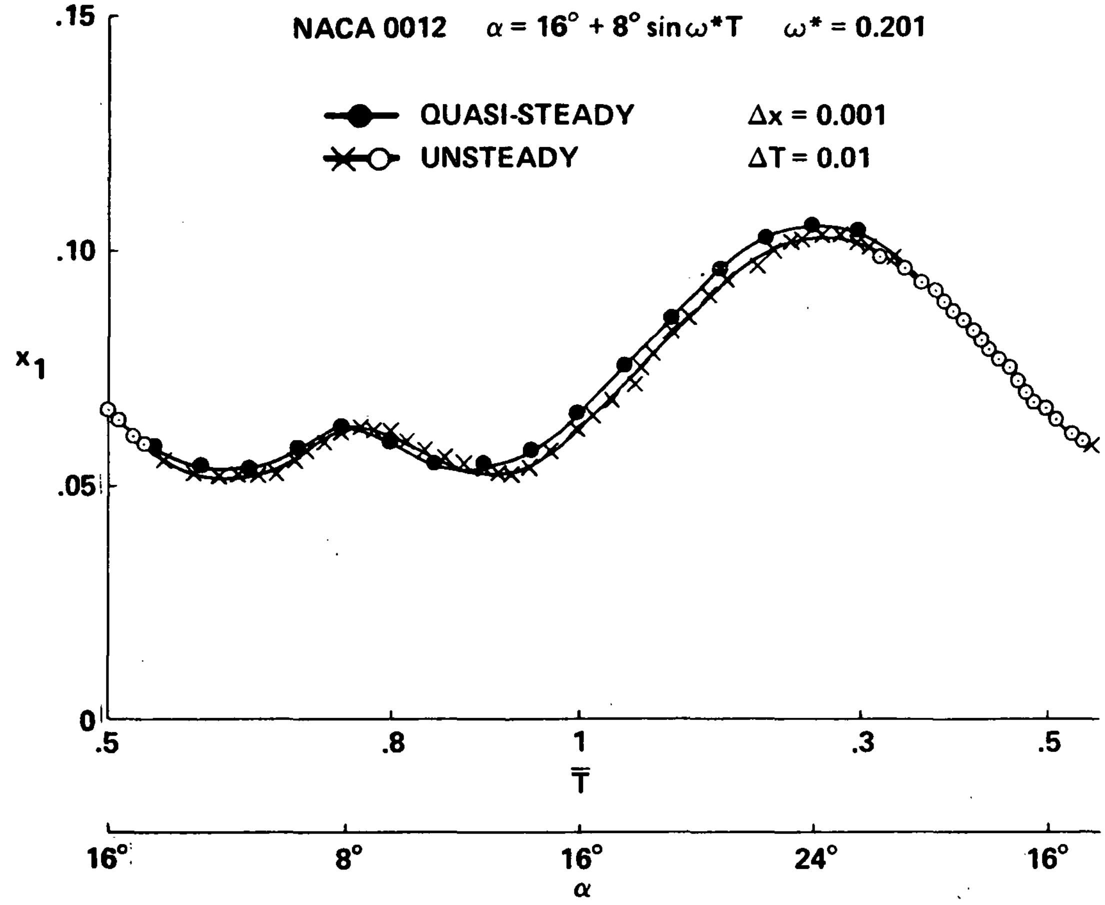

Figure 33.- Quasi-steady and unsteady separation lines over a period of oscillation: case C, α_0 = 16°.

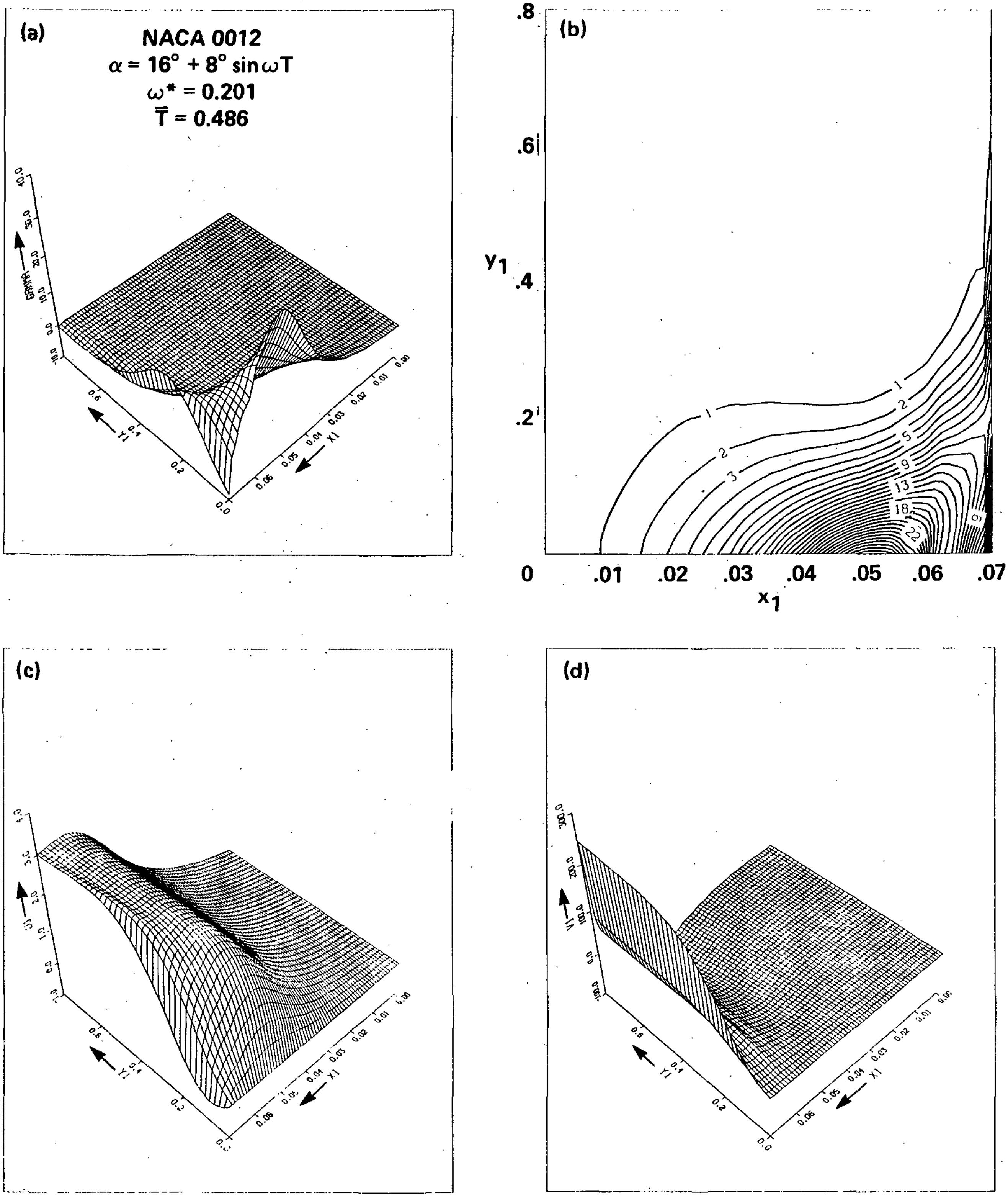

Figure 34.- Vorticity and velocity distributions with respect to x_1, close to separation.

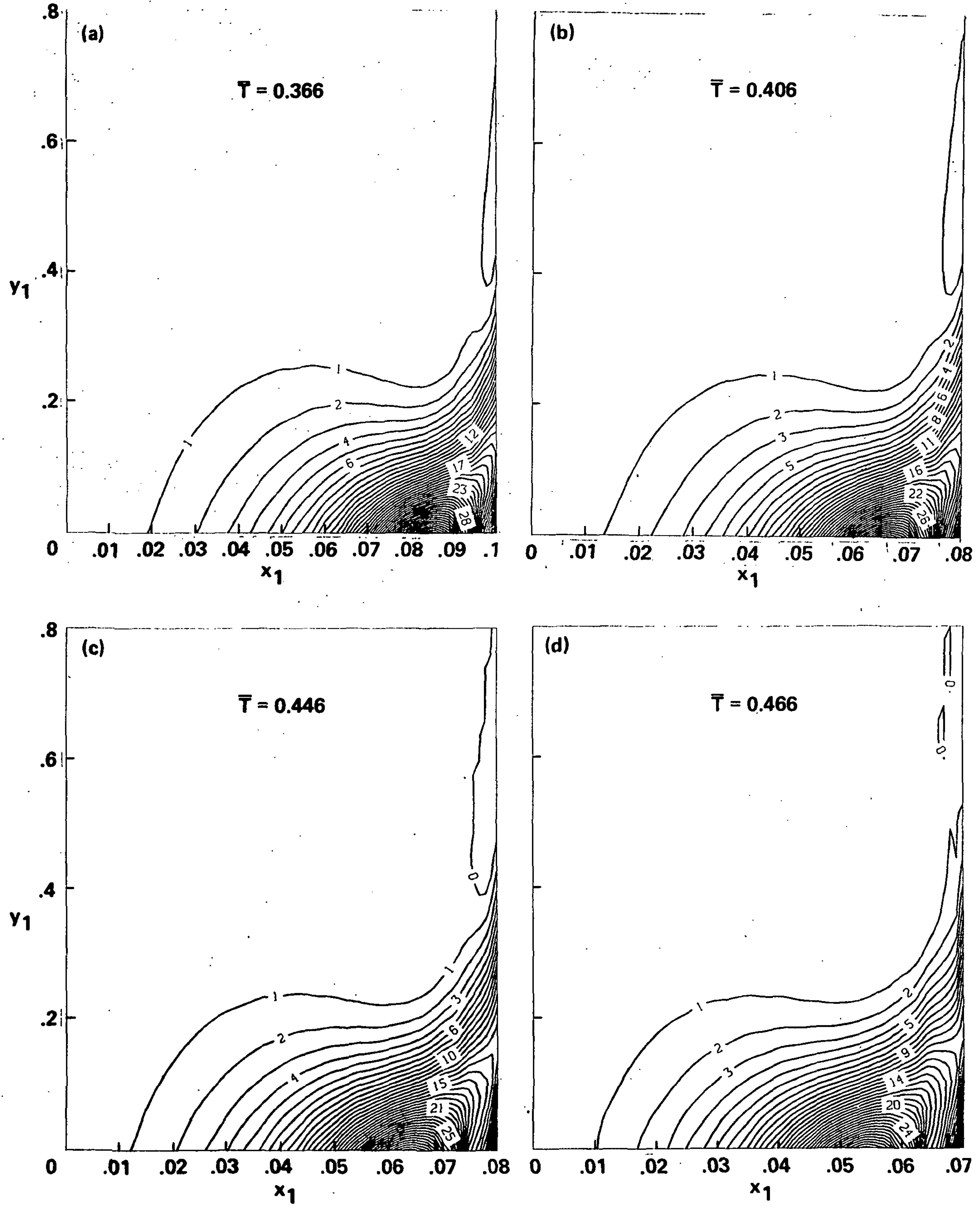

Figure 35.- Vorticity contours with respect to x_1: case C, $\alpha_0 = 16°$ ($\omega^* = 0.2$).

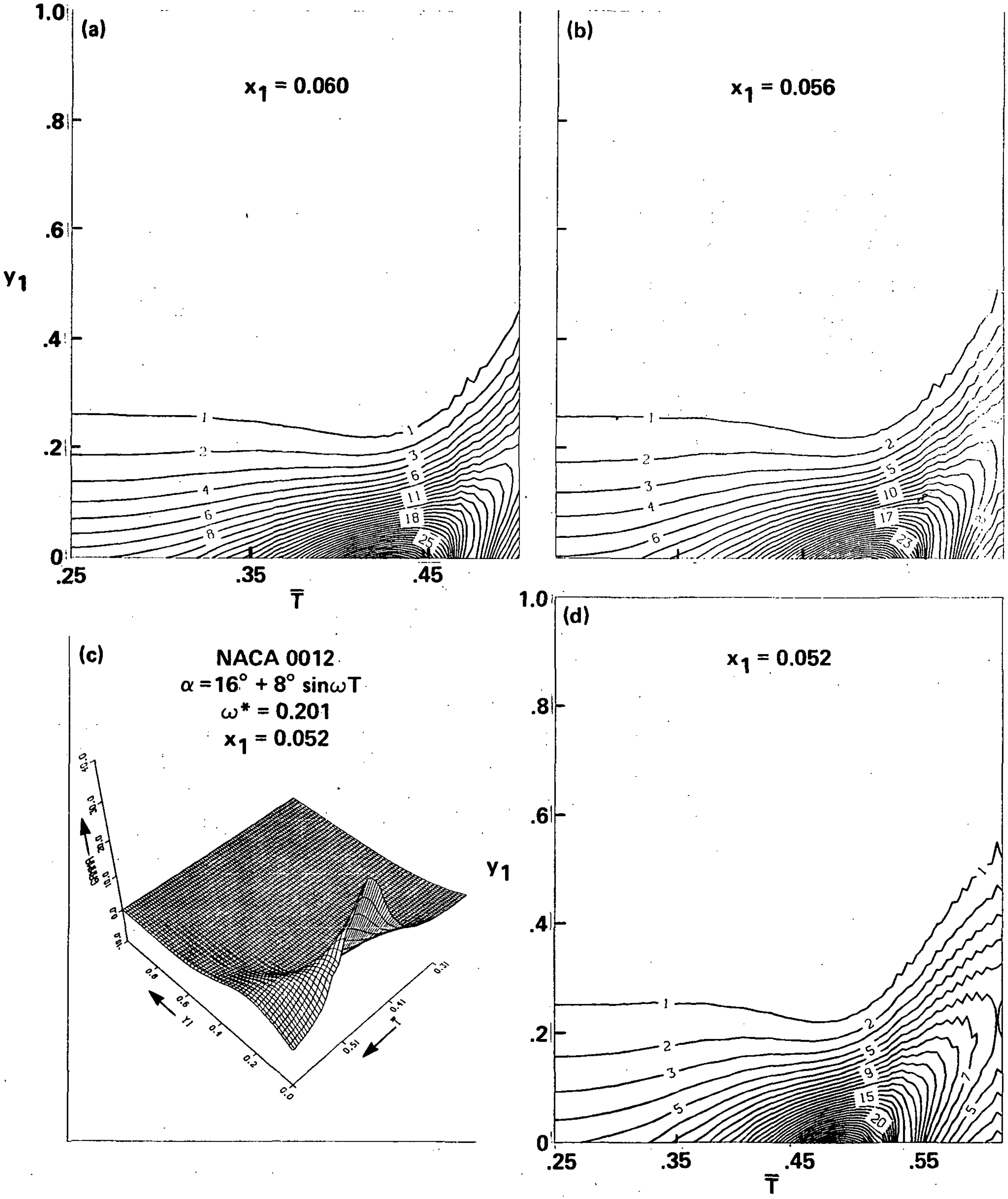

Figure 36.- Contour plots and three-dimensional plot of vorticity: case C, α_0 = 16° (ω^* = 0.2).

1. Report No.
NASA TM-84319

2. Government Accession No.

3. Recipient's Catalog No.

4. Title and Subtitle UNSTEADY LAMINAR BOUNDARY LAYER CALCULATIONS ON OSCILLATING CONFIGURATIONS INCLUDING BACKFLOW. PART II: AIRFOIL IN HIGH-AMPLITUDE PITCHING MOTION – DYNAMIC STALL

5. Report Date
July 1983

6. Performing Organization Code

7. Author(s)
W. Geissler

8. Performing Organization Report No.
A-9403

9. Performing Organization Name and Address
NASA Ames Research Center
Moffett Field, Calif. 94035

10. Work Unit No.
T-34144

11. Contract or Grant No.

12. Sponsoring Agency Name and Address
National Aeronautics and Space Administration
Washington, D.C. 20546

13. Type of Report and Period Covered
Technical Memorandum

14. Sponsoring Agency Code
505-42-21

15. Supplementary Notes
Point of Contact: L. W. Carr, Ames Research Center, MS 227-8, Moffett Field, CA 94035. (415) 965-6265 or FTS 448-6265.

16. Abstract

A previously developed finite-difference procedure for calculating unsteady, incompressible, laminar boundary layers on an oscillating flat plate is applied to a wing section undergoing high-amplitude pitching oscillations about various mean incidences. To start the entire boundary-layer calculation, appropriate initial conditions and outer boundary conditions are specified, using a stagnation-point fixed frame of reference. The breakdown of the numerical calculation procedure in the x,t-domain is interpreted to coincide with unsteady separation. Details of the boundary-layer behavior in the vicinity of separation are investigated, and a close analogy between the present results and those for a three-dimensional steady separation is found.

17. Key Words (Suggested by Author(s))
Unsteady viscous flow
Boundary layers
Separating flow
Reversed flow

18. Distribution Statement
Unlimited

Subject Category - 02

19. Security Classif. (of this report)
Unclassified

20. Security Classif. (of this page)
Unclassified

21. No. of Pages
55

22. Price*
A04

*For sale by the National Technical Information Service, Springfield, Virginia 22161